

ADP-00-48/T429

# COLOR COHERENT PHENOMENA ON NUCLEI AND THE QCD EVOLUTION EQUATION

Leonid Frankfurt

*Sackler School of Physics and Astronomy*

*Tel Aviv University, Ramat Aviv*

*Tel Aviv, Israel*

Vadim Guzey

*The Pennsylvania State University*

*University Park, PA, USA;*

*Special Research Centre for the Subatomic Structure of Matter (CSSM),*

*Adelaide University , Australia, 5005*

and

Mark Strikman

*The Pennsylvania State University*

*University Park, PA, USA*

## Abstract

We review the phenomenon of color coherence in quantum chromodynamics (QCD), its implications for hard and soft processes with nuclei, and its experimental manifestations. The relation of factorization theorems in QCD with color coherence phenomena in deep inelastic scattering (DIS) and color coherence phenomena in hard exclusive processes is emphasized. Analyzing numerically the QCD evolution equation for conventional and skewed parton densities in nuclei, we study the onset of generalized color transparency and nuclear shadowing of the sea quark and gluon distributions in nuclei as well as related phenomena. Such novel results as the dependence of the effective coherence length on  $Q^2$  and general trends of the QCD evolution are discussed. The limits of the applicability of the QCD evolution equation at small Bjorken  $x$  are estimated by comparing the inelastic quark-antiquark- and two gluon-nucleon (nucleus) cross sections, calculated within the DGLAP approximation, with the dynamical boundaries, which follow from the unitarity of the  $S$  matrix for purely QCD interactions. We also demonstrate that

principles of color coherence play an important role in the processes of soft diffraction off nuclei.

## I. INTRODUCTION

The aim of this review article is to summarize fundamental principles of color coherent phenomena in quantum chromodynamics (QCD) and to apply these principles to the calculation of cross sections of diffractive processes at high energy, where color coherence plays a crucial role.

Our goal is threefold. Firstly, we make an attempt to give a comprehensive and pedagogical overview of main ideas which constitute the concept of color coherence in QCD. In the preparation of this part, we have benefited from review articles [1,2], a talk [3], and a series of lectures [4].

Secondly, we discuss hard exclusive diffractive processes. The recent proof of the factorization theorem for hard exclusive diffractive electroproduction of mesons [5] justifies the computation of the amplitude of this reaction in terms of the skewed parton densities [5,6]. In the present work, we analyze numerically the onset of generalized color transparency in hard exclusive diffractive processes and the phenomenon of nuclear shadowing in total cross sections in deep inelastic scattering (DIS) using the QCD evolution equation for the skewed and conventional nuclear parton densities. We also estimate the limits of the applicability of the DGLAP QCD evolution equation by comparing the calculated inelastic and elastic scattering cross sections of spatially small quark and gluon dipoles off the nucleon or nucleus with the dynamical boundaries, which follow from the unitarity of the  $S$  matrix for purely QCD interactions [7]. We demonstrate that studies of a new QCD regime, color opacity, may be feasible with future electron-nucleus colliders and in special hard processes in  $ep$  collisions at HERA.

Thirdly, we review the soft diffraction of hadrons on light and heavy nuclei. We demonstrate that the principles of color coherence form the ground for the adequate phenomenological description of the available data on hadron-nucleus coherent diffractive dissociation.

The phenomenon of color coherence in QCD has two principal features: 1) an energetic projectile (hadron or photon) consists of coherent quark-gluon configurations of very different transverse spatial sizes; 2) a small-size quark-gluon configuration has reduced interactions with the target at not very small  $x$ .

The coherent quark-gluon configurations, which constitute the energetic projectile, are called color fluctuations because QCD color occupies different volumes for the configurations of different transverse sizes. Phenomenon 2) is called color screening. Both aspects of color coherence have been proven in perturbative QCD (pQCD) and have been observed experimentally. Since configurations of various transverse sizes are present in the projectile at high energies, studies of color coherence phenomena provide an important relation between hard physics (small-size quark-gluon fluctuations), which is quite well understood in terms of QCD, and soft physics (large-size quark-gluon fluctuations), which is treated mostly phenomenologically.

Property 1 is based on the observation that at high energies the longitudinal distance, essential for a given process, increases with the increase of energy. Originally, before QCD was known, such a behaviour of high-energy hadron collisions was suggested in [8–11]. The

longitudinal distance is called coherence length  $l_c$  [12]. The word *coherence* reflects the attribute of any quantum field theory, which consists in the fact that particles are predominantly radiated at large and increasing with energy distances because of Lorentz slowing down of interactions.

Property 1 is well understood in quantum electrodynamics [13]. Coherence length  $l_c$  also exists in pQCD where it also increases with energy. It can be easily proven that this property of  $l_c$  is a consequence of gauge invariance and the renormalizability of QCD. The convergence of integrals over “masses” of the intermediate states in the wave function of the incoming virtual photon follows from the absence of ultraviolet divergencies in the amplitudes, except where it is related to the renormalization of the coupling constant. However, in QCD this convergence is rather slow, which leads to the  $Q^2$  dependence of the coherent phenomena, discussed in this review. This  $Q^2$  dependence can also be understood as a result of the slow  $Q^2$  dependence of the effective coherence length, introduced in the present paper.

The large coherence length allows the presence of many quark-gluon coherent fluctuations of various transverse sizes in the energetic projectile. The latter results in a large probability of coherent diffractive processes, experimentally observed at HERA [14], and leading twist nuclear shadowing in DIS, experimentally observed for light nuclei [15] and heavy ones [16] at CERN. Below we shall consider the relationship between the large  $l_c$  and the experimental results in more detail.

Let us consider diffractive DIS scattering of a photon with virtuality  $Q^2$ , energy  $q_0$ , and high momentum  $q$  on a hadronic target  $T$  in the reaction  $\gamma^* + T \rightarrow X + T'$ . The coherence length  $l_c$  is introduced as the time (distance) for which the incoming virtual photon exists as quark-gluon fluctuations with the average mass squared  $\langle M_X^2 \rangle$ . It follows from the uncertainty principle that

$$l_c = \frac{1}{\Delta E} = \frac{1}{\sqrt{q^2 + \langle M_X^2 \rangle} - q_0} \simeq \frac{2q}{\langle M_X^2 \rangle + Q^2}, \quad (1)$$

where  $m_N$  is the nucleon mass. In Eq. (1) one often uses the approximation  $\langle M_X^2 \rangle = Q^2$  and arrives at

$$l_c \simeq \frac{1}{2m_N x}, \quad (2)$$

where  $x$  is the Bjorken variable [9]. In Subsect. II B we shall explain that since coherence of high energy processes is realized through diffractive processes, the parton model approximation  $\langle M_X^2 \rangle = Q^2$  is no longer valid if one takes into account the effects of the QCD evolution. Then, more appropriate quantities are the effective coherence length  $l_c^{eff}$  defined by Eq. (1), where  $M_X^2$  is the typical mass in diffractive processes in DIS.

Let the coherence length of Eq. (1) be larger than the typical size of the target

$$l_c > 2R_T, \quad (3)$$

where  $R_T$  is the radius of the target. Then, not only are all quark-gluon fluctuations, satisfying Eq. (3), present in the photon wave function and interact coherently with the target  $T$ , but the target also has a large probability of remaining in the ground state. This fact leads to a large probability of coherent (when the nucleon or nuclear target is left intact during the interaction) diffractive processes on nucleons and nuclei.

In inclusive DIS on nuclei, when Eq. (3) holds, the incoming virtual photon interacts coherently with several nucleons of the nucleus. This manifests itself in nuclear shadowing. The QCD-improved aligned jet model, which takes into account the interplay between soft and hard physics [17], explicitly demonstrates that shadowing should be of the leading twist, i.e. only the logarithmic decrease of the effect of shadowing with increasing  $Q^2$  is allowed. Note that at sufficiently small  $x$  the very concept of decomposition over twists might appear inapplicable to QCD. We refer the reader to Subsect. IV C for the relevant discussion.

Property 2) of color coherence, color screening, has been proved in pQCD using gauge invariance, asymptotic freedom, and the QCD factorization theorem. The suppression of the interaction of small-size quark-gluon configurations of incoming hadrons and photons with hadronic targets leads to several distinctive experimental signatures of color coherence. In nuclear quasi-elastic reactions, where small-size configurations are produced as a result of high  $Q^2$  two-body wide-angle scattering, the suppression of initial and final state interactions is called color transparency [18,19]. In QED, a similar phenomenon of “the electric neutrality” was theoretically predicted in as early as 1954 by H. Bethe and L. Maximon [20] by considering coherent production of  $e^+e^-$  pairs in photon-nucleus scattering within the eikonal approximation<sup>1</sup>. Note that one can justify the applicability of the eikonal approximation in QED, while, in QCD, the validity of this approximation is questionable even in the perturbative regime because of “strong” gluon-gluon interactions. In hard diffractive processes, like the electroproduction of vector mesons off nucleons and nuclei, the interaction becomes strong at sufficiently small  $x$ ,  $x \leq 0.01$ , and one reaches the regime of perturbative color opacity [21,22]. In this regime, the suppression in the amplitude is explained by nuclear shadowing of gluons and, hence, the factorization theorem is still valid. Therefore, the regime of perturbative color opacity can be also called the regime of generalized color transparency. We demonstrate that, in the limit of fixed  $x$  and  $Q^2 \rightarrow \infty$ , the generalized color transparency is reduced to color transparency. At sufficiently small  $x$ , the interaction becomes strong, which leads to violation of the factorization theorem, and, possibly, to different nuclear shadowing in hard inclusive and hard exclusive processes.

Perturbative QCD causes a particular energy and  $Q^2$  behaviour of the differential cross section of the hard vector meson production. This behaviour has been verified experimentally (see discussion of relevant HERA experiments in [14]). Color transparency has recently been observed directly in the diffractive excitation of pions into two jets off nuclear targets [23], in line with the predictions of [22]. A number of other processes such as  $J/\psi$  photoproduction, leading hadron production in nuclear reactions using Drell-Yan lepton pairs as a trigger, and the production of leading nucleons in nucleus-nucleus collisions can be understood and confronted with the experimental data only if the coherent nature of the reactions is taken into account.

This review is organized in the following way. Sect. II is concerned with cornerstones of the theoretical treatment of color coherent phenomena in QCD. These are the dynamics of small objects and the factorization theorems. We also discuss the relationship between diffraction on the proton in the reaction  $\gamma^* + p \rightarrow X + p'$  and nuclear shadowing in DIS scattering  $\gamma^* + A \rightarrow X$ . We critically examine the definition of the coherence length and

<sup>1</sup>We are indebted to S. Brodsky who drew our attention to [20].

present the  $Q^2$  dependence of the effective coherence length  $l_c^{eff}$ . We also review the aligned jet model of Bjorken and explain the improvements of this model which are to be done to make it conform with QCD [17].

In Sect. III, the principles of color coherence in QCD are applied to exclusive hard diffractive processes. The main features of generalized color transparency are reviewed. We also discuss experiments, in which color coherence plays a crucial role. New reactions, where the two-gluon exchange is prohibited but color transparency still holds, are proposed.

Sect. IV quantitatively illustrates our conclusions concerning the transition from generalized color transparency to color transparency at fixed  $x$  and  $Q^2 \rightarrow \infty$ , and concerning the behaviour of parton densities in nuclei by the virtue of analyzing the QCD evolution of skewed and conventional nuclear parton densities. A study of general trends of the QCD evolution in the  $x - Q$ -plane is presented. We also study the limits of applicability of the leading twist DGLAP evolution equation at small Bjorken  $x$  using the unitarity of the  $S$ -matrix for purely QCD interactions as a guiding principle [7].

In Sect. V, we give an overview of soft hadron diffraction on nuclei from the point of view of color coherence. We demonstrate that the formalism, which takes into account color fluctuations of hadronic projectiles explicitly, gives a universal description of the available data on diffractive dissociation and nuclear shadowing for light and heavy nuclei.

## II. COLOR COHERENCE IN DIFFRACTIVE PROCESSES

The investigation of the role of color coherent phenomena in inclusive, exclusive and semi-exclusive high energy processes is one of the rapidly developing fields in QCD. Many calculations can be done in pQCD with the use of the dynamics of small-size quark-gluon configurations and the factorization theorems in a model-independent way.

We begin this section by reviewing a deep relationship between nuclear shadowing in inclusive DIS on nuclei and DIS diffraction on protons, which is based on the factorization theorem for DIS diffraction  $\gamma^* + p \rightarrow X + p'$  [24].

### A. Leading twist nuclear shadowing and diffraction in DIS

A deep connection between high energy diffraction and the phenomenon of nuclear shadowing was first understood by V. Gribov [10,25]. On the qualitative level, nuclear shadowing in DIS on the lightest nucleus, deuterium, arises from the interference between the amplitudes for diffractive scattering of the projectile off the proton and the neutron of the deuterium target. This is presented schematically in Fig. 1. The application of the cutting rules of Abramovskii, Gribov, and Kancheli [26] explicitly demonstrates that the interference diagram decreases the total cross section for  $\gamma^*D$  scattering, i.e. it leads to nuclear shadowing.

One can use this result in order to calculate the modification of parton densities in nuclei at low values of Bjorken  $x$ . By comparing the QCD diagrams for hard diffraction and for nuclear shadowing due to scattering off two nucleons (see Fig. 1), one can prove [27] that, in the limit of low nuclear thickness, nuclear shadowing of nuclear parton densities

$f_{j/A}(x, Q^2)$  is unambiguously expressed through diffractive parton densities in the proton  $f_{j/N}^D(\beta, Q^2, x_{IP}, t)$

$$f_{j/A}(x, Q^2)/A = f_{j/N}(x, Q^2) - \frac{1}{2} \int d^2 b \int_{-\infty}^{\infty} dz_1 \int_{z_1}^{\infty} dz_2 \int_x^{x_0} dx_{IP} \\ \times \frac{1 - \eta^2}{1 + \eta^2} f_{j/N}^D(\beta, Q^2, x_{IP}, t) \Big|_{k_t^2=0} \rho_A(b, z_1) \rho_A(b, z_2) \cos(x_{IP} m_N(z_1 - z_2)) , \quad (4)$$

where  $f_{j/N}(x, Q^2)$  is the conventional parton density in the proton;  $\rho_A(r)$  is the nucleon density in the nucleus with atomic number  $A$ ;  $x_{IP}$  is the fraction of the proton longitudinal momentum carried by the Pomeron;  $t$  is the momentum transfer, defined as  $-t = (k_t^2 + (x_{IP} m_N)^2)/(1 - x_{IP})$ , where  $k_t$  is the transverse component of the momentum, transferred to the struck nucleon;  $\beta = x/x_{IP}$ ;  $x_0 \simeq 0.02$ . In Eq. (4), the factor  $(1 - \eta^2)/(1 + \eta^2)$ , where  $\eta = -\pi/2 \partial \ln(\sqrt{f_{j/N}})/\partial \ln(1/x_{IP}) = \pi/2 \kappa$  accounts for the real part of the amplitude for the diffractive scattering [28]. The experimental value of the parameter  $\kappa$ , defined as  $f_{j/N}^D(\beta, Q^2, x_{IP}, t) \Big|_{k_t^2=0} \propto x_{IP}^{2\kappa}$ , is rather small,  $\kappa \approx 0.15$ .

Considering deuteron, one can write a compact expression, which includes the  $t$  dependence of the electromagnetic form factor  $F_{2H}(q)$ , where  $-t = q^2$

$$f_{j/2H}(x, Q^2)/2 = f_{j/N}(x, Q^2) - \frac{1}{8\pi} \int_x^{x_0} dx_{IP} d^2 t \frac{1 - \eta^2}{1 + \eta^2} f_{j/N}^D(\beta, Q^2, x_{IP}, t) F_{2H}(4t) . \quad (5)$$

Similarly to Eq. (5), one can easily generalize Eq. (4) in order to include the dependence of the diffractive amplitude on  $t$  ( see, e.g., [29]).

The factorization theorem for DIS diffraction  $\gamma^* + p \rightarrow X + p'$  [24] states that the diffractive parton densities at fixed  $x_{IP}$  and  $t$  are described by the leading twist DGLAP QCD evolution equation. Therefore, the nuclear shadowing, described by Eq. (4), is also a leading twist effect and is governed by the DGLAP QCD evolution equation [27].

Thus, Eq. (4) should be understood as the initial condition for the QCD evolution for the nuclear parton densities. Since Eq. (4) is valid at low  $x$ , in particular at  $l_c^{eff} > 2R_A$ , where  $R_A$  is the nuclear radius (see Eq. (3)), the nuclear effects typical for larger  $x$  are absent in Eqs. (4) and (5). A slight enhancement of gluon and valence quark parton densities in the nucleus at  $x \approx 0.1$  should be added to Eqs. (4) and (5) at some initial evolution scale  $Q_0$ . At larger  $Q$ , this enhancement will contribute at much smaller  $x$  and will diminish the effect of nuclear shadowing. This simple argument shows that nuclear shadowing should decrease logarithmically as  $Q$  increases due to the QCD evolution due to two effects: decreasing  $l_c^{eff}$  with increasing  $Q^2$  and the growing contribution of the enhancement region  $x \geq 0.1$ .

Eq. (4) can be used to study the amount of nuclear shadowing for quark and gluon parton densities separately. The analysis of [27] showed that: i) there is significant shadowing for quark parton densities with small theoretical uncertainties; ii) nuclear shadowing for gluon parton densities is larger by approximately a factor of 3 than for the quark parton densities<sup>2</sup>.

---

<sup>2</sup>Note that this result was derived in the approximation of the low nuclear thickness. Hence, it is valid for light nuclei only. For heavy nuclei, it is necessary to account for the interaction of  $\gamma^*$  with

Fig. 2 presents the amount of nuclear shadowing at small  $x$  for the ratio of nuclear and nucleon gluon parton densities  $G_A/AG_N$  and for the ratio of nuclear and nucleon quark parton densities  $q_A/Aq_N$  for the nuclei of lead (Pb) and carbon (C). At the initial scale of the QCD evolution  $Q_0=2$  GeV, the nuclear shadowing corrections were calculated using Eq. (4) as well as taking into account the higher order rescattering terms. The dashed, dotted and solid curves correspond to  $Q=2, 5$  and  $10$  GeV, respectively. One can see from Fig. 2 that at the initial QCD evolution scale  $Q=2$  GeV, nuclear shadowing for gluons is larger by approximately a factor of 3 than for quarks. As explained above, due to the QCD evolution, nuclear shadowing for the ratio  $G_A/AG_N$  becomes significantly reduced at  $Q=5$  and  $10$  GeV and is compatible to nuclear shadowing for  $q_A/Aq_N$ .

Note that, in many models of nuclear shadowing which do not use the information about gluon-induced diffraction, it is expected that gluons are shadowed less than quarks. Also, in a number of models, the interaction of small dipoles with several nucleons is considered in the eikonal approximation. However, by comparing Eq. (4) and the expression based on the eikonalization of the pQCD cross section for the interaction of a small-size dipole with a single nucleon (Eq. (13)), it is easy to check that the leading twist coupling of the small-size dipole to two nucleons, presented in Fig. 1, gives significantly larger shadowing than the higher twist eikonal diagrams, where four gluons are attached to a  $q\bar{q}$  dipole. For example, at  $Q^2=10$  GeV $^2$  and  $x = 10^{-3}$ , nuclear shadowing, calculated using Eq. (4), is larger by a factor 3 than nuclear shadowing, calculated in the eikonal approximation. Hence, the eikonal approximation strongly underestimates the strength of nuclear shadowing for the interaction of small dipoles. In particular, for the total photoabsorption cross section of longitudinally polarized virtual photons  $\sigma_L$ , Eq. (4) corresponds to the leading twist shadowing for gluons, while calculations, using the eikonal approximation, predict higher twist nuclear shadowing, which is much smaller numerically, cf. [7].

At the same time, it was recently shown [30] that a model, which incorporated the Gribov theory of nuclear shadowing and HERA diffractive data, successfully described the high precision NMC data on nuclear structure functions at low  $x$  [15,16].

In the laboratory reference frame, nuclear shadowing is controlled by Eq. (4) and by the coherence length  $l_c$ . In the next subsection we shall review the definition of  $l_c$  and analyze its  $Q^2$  dependence within the framework of the factorization theorem [24] and the QCD evolution equation.

## B. $Q^2$ dependence of the effective coherence length

It is evident from Eq. (4) that the leading contribution to nuclear shadowing in DIS on nuclear targets is proportional to the diffractive differential cross section at the minimal momentum transfer  $t_{min}$ . Also, diffraction plays a dominant role in the generalized color transparency phenomenon. Thus, it is useful to introduce the notion of the effective co-

---

3, 4, ... nucleons of the target. Also, we have checked that the use of the diffractive parton densities obtained by Hautmann, Kunszt and Soper, based on the calculations in perturbative QCD at the initial scale  $Q_0=1.5$  GeV [84], lead to very similar numerical results.

herence length  $l_c^{eff}$ . By definition  $l_c^{eff}$  is the coherence length, which controls the onset of the nuclear shadowing and generalized color transparency phenomena. The definition of the coherence length  $l_c$ , given by Eq. (2), is based on the parton model assumption that  $\langle M_X^2 \rangle \approx Q^2$ . This approximation is valid only at moderate  $Q^2$  and  $x \sim 10^{-2} \div 10^{-3}$ . As  $Q^2$  increases, the ratio  $\langle M_X^2 \rangle / Q^2$  increases logarithmically at fixed  $x$  due to the QCD evolution. This effect becomes even more important at very small  $x$  due to the presence of  $\alpha_s \ln(1/x)$  effects.

According to the discussion in the Introduction,  $\langle M_X^2 \rangle$  should be understood as the average mass squared of the diffractively produced final state  $X$  in the single-diffractive scattering process  $\gamma^* + T \rightarrow X + T'$ . Thus, in order to study the  $Q^2$  dependence of  $l_c^{eff}$ , one should determine the typical masses  $\langle M_X^2 \rangle$ , which give the dominant contribution to the diffractive differential cross section  $d\sigma^D/dt(t = t_{min})$  of the process  $\gamma^* + T \rightarrow X + T'$ , where  $-t_{min} \approx (x_{IP} m_N)^2$ .

The diffractive differential cross section  $d\sigma^D/dt(t = t_{min})$  can be written as

$$\frac{d\sigma^D}{dt}(t = t_{min}) \equiv \frac{d^3\sigma^D}{dx dQ^2 dt}(t = t_{min}) = \frac{2\pi\alpha^2}{xQ^4} (1 + (1 - y)^2) \int_x^{0.02} dx_{IP} F_2^{D(4)}(x, Q^2, x_{IP}, t_{min}) , \quad (6)$$

where  $F_2^{D(4)}(x, Q^2, x_{IP}, t)$  is the diffractive structure function;  $y$  is the rapidity. For simplicity, the longitudinal structure function is neglected in Eq. (6). The Pomeron model of diffractive processes is supposed to be valid at small  $x_{IP}$ . We followed the prescription of Ref. [27] and set the upper limit of integration in Eq. (6) to 0.02. However, our numerical analysis is not too sensitive to the particular choice of the upper limit – a variation of the upper limit between 0.01 and 0.03 changes the result for  $l_c^{eff}$  by less than 25%.

The factorization theorem for diffractive DIS scattering [24] states that one can introduce the diffractive parton densities for fixed  $x_{IP}$  and  $t$ , which satisfy the usual DGLAP evolution equation. The leading twist contribution to  $F_2^{D(4)}(x, Q^2, x_{IP}, t)$  can be expressed through these parton densities. In practical applications, a further simplifying assumption is made – for sufficiently small  $x_{IP} \leq 0.02$ , where the vacuum pole exchange dominates, one can write  $F_2^{D(4)}(x, Q^2, x_{IP}, t)$  in the factorized form

$$F_2^{D(4)}(x, Q^2, x_{IP}, t) = f_{IP/p}(x_{IP}, t) F_2^{D(2)}(\beta, Q^2) , \quad (7)$$

where  $f_{IP/p}(x_{IP}, t)$  is the Pomeron flux;  $F_2^{D(2)}(\beta, Q^2)$  is the diffractive structure function;  $\beta$  is the fraction of the Pomeron momentum carried by partons inside the Pomeron defined as  $\beta = x/x_{IP}$ . Substituting Eq. (7) in Eq. (6), one obtains

$$\begin{aligned} \frac{d\sigma^D}{dt}(t = t_{min}) &= \frac{2\pi\alpha^2}{xQ^4} (1 + (1 - y)^2) \int_x^{0.02} dx_{IP} f_{IP/p}(x_{IP}, t_{min}) F_2^{D(2)}\left(\frac{x}{x_{IP}}, Q^2\right) \\ &= \frac{2\pi\alpha^2}{xQ^4} (1 + (1 - y)^2) \int_{x/0.02}^1 \frac{d\beta}{\beta^2} x f_{IP/p}\left(\frac{x}{\beta}, t_{min}\right) F_2^{D(2)}(\beta, Q^2) . \end{aligned} \quad (8)$$

In order to use Eq. (8) for studying  $l_c^{eff}$  and  $M_X^2$  as a function of  $Q^2$ , let us notice that  $M_X^2$  is kinematically related to  $\beta$  as

$$\beta = \frac{Q^2}{Q^2 + M_X^2} . \quad (9)$$

This equation demonstrates that, at fixed by the kinematics of the reaction  $Q^2$  and  $x$ , the averaging over diffractive masses  $M_X$  in Eq. (1) is equivalent to the averaging over  $\beta$ . Substituting Eq. (9) into (1) we obtain

$$l_c^{eff} = \frac{1}{m_N x} \langle \beta \rangle(Q^2, x) . \quad (10)$$

$\langle \beta \rangle(Q^2, x)$  is the typical value of  $\beta$ , which dominates the integral in Eq. (8). It depends on  $Q^2$  and  $x$ . The  $Q^2$  dependence of  $\langle \beta \rangle(Q^2, x)$  is governed by the DGLAP QCD evolution of the diffractive parton densities, which enter  $F_2^{D(2)}(\beta, Q^2)$ . The  $x$  dependence of  $\langle \beta \rangle(Q^2, x)$  comes from the  $x$  dependence of the lower limit of integration and the Pomeron flux in Eq. (8).

We propose the following ansatz for the evaluation of  $\langle \beta \rangle(Q^2, x)$ . At each  $x$  and  $Q$ ,  $\langle \beta \rangle(Q^2, x)$  is given by the median of the integral in Eq. (8)

$$\frac{1}{2} \int_{x/0.02}^1 \frac{d\beta}{\beta^2} f_{P/p}(\frac{x}{\beta}, t_{min}) F_2^{D(2)}(\beta, Q^2) = \int_{x/0.02}^{\langle \beta \rangle(Q^2, x)} \frac{d\beta}{\beta^2} f_{P/p}(\frac{x}{\beta}, t_{min}) F_2^{D(2)}(\beta, Q^2) . \quad (11)$$

Thus, solving Eq. (11) for  $\langle \beta \rangle(Q^2, x)$  will give the desired  $Q^2$  dependence of  $l_c^{eff}$  through Eq. (10).

In our analysis of Eq. (11), we used the leading order expression for the diffractive structure function  $F_2^{D(2)}(\beta, Q^2)$

$$F_2^{D(2)}(\beta, Q^2) = \sum_a e_a^2 \beta q_a(\beta, Q^2) , \quad (12)$$

where  $q_a(\beta, Q^2)$  is the parton density of a quark with flavor  $a$  inside the Pomeron;  $e_a$  is the charge of the quark.

The  $Q^2$  dependence of  $q_a(\beta, Q^2)$  was studied using the next-to-leading order (NLO) DGLAP QCD evolution equation. The recent parameterization of diffractive parton densities of Ref. [31] was used as an input for the QCD evolution. We choose the fit **D**, which gives the best description of the diffractive DIS and photoproduction data from HERA. All fits of [31] correspond to the initial scale  $Q_0=2$  GeV. At this scale, the gluon density is non-zero,  $u(x) = d(x) = \bar{u}(x) = \bar{d}(x) \neq 0$ , and  $s(x) = \bar{s}(x) = 0$ . As one performs the QCD evolution to larger  $Q > Q_0$ , the equality  $u(x) = d(x) = \bar{u}(x) = \bar{d}(x)$  remains and strange quarks  $s(x) = \bar{s}(x) \neq 0$  are generated.

The current HERA data does not cover the region of small  $\beta$  at small  $x$ , hence the fits of [31] are not sensitive to the region where the triple Pomeron contribution dominates. In order to explore the sensitivity of the value of  $l_c^{eff}$  to this region, we have included the small- $\beta$  contribution, using the limiting fragmentation ansatz of Ref. [32]. In the limit of small  $\beta$  and at  $Q^2 = Q_0^2$ , the multiplicity of leading hadrons in the target fragmentation region approximately coincides with that in photoproduction. This prediction is consistent with recent HERA data at  $x_{IP} \geq 0.05$ .

In Fig. 3 we present  $l_c^{eff} m_N x = \langle \beta \rangle(Q^2, x)$  as a function of  $Q$  at  $x=10^{-4}$ ,  $10^{-3}$ , and  $10^{-2}$ , calculated using Eqs. (10) and (11) with (dashed lines) and without (solid lines)

small- $\beta$  contribution. One can see that, at each  $x$ , the coherence length  $l_c^{eff}$  is a decreasing function of  $Q$ . Also, one observes that the small- $\beta$  tail becomes increasingly important with decreasing  $x$ , especially at  $Q^2 \sim Q_0^2$ .

Using Fig. 3, one can also study the  $x$  dependence of  $l_c^{eff}$  at given  $Q^2$ . While  $l_c^{eff}$  increases as  $x$  decreases, this increase is slower than  $1/x$  behaviour predicted by Eq. (2). Also, the difference between  $l_c^{eff}$  for different  $x$  becomes larger as  $Q^2$  increases. These effects are attributed to the QCD evolution of diffractive parton densities.

Note that the definition of  $l_c^{eff}$ , which uses Eqs. (10) and (11), is less reliable at large Bjorken  $x$ ,  $x \geq 0.01$ , since the diffractive cross sections are quite small at those  $x$ .

We would like to stress that a decrease of  $l_c^{eff}$  with increasing  $Q$  is a model-independent statement. It is a direct consequence of the factorization theorem in diffractive DIS and the QCD evolution of diffractive parton densities. As  $Q$  increases, the parton densities become softer, i.e. they shift towards lower  $\beta$  (or higher  $M_X$  according to Eq. (9)). Hence, at fixed  $x$ ,  $\langle \beta \rangle(Q^2, x)$  decreases as  $Q$  is increased, or, alternatively,  $\langle M_X^2 \rangle$  increases as  $Q$  is increased. Hence, by virtue of Eq. (1)  $l_c^{eff}$  decreases with  $Q$ .

Such a behaviour of the effective coherence length is supported by the experiment. The ZEUS data on single-diffraction [33] demonstrates that as  $Q^2$  increases, diffractive states of large mass become increasingly important [34]. Hence, according to Eq. (1), the effective coherence length should decrease as  $Q^2$  increases due to increasing  $\langle M_X^2 \rangle$  with  $Q^2$ .

In conclusion, we would like to point out that the present-day knowledge of diffractive quark and gluon parton densities enables one to evaluate the leading twist contribution to nuclear shadowing in the quark and gluon channels separately. In the nuclear rest frame, the quark channel corresponds to quark-antiquark fluctuations of the incoming virtual photon, while the gluon channel can be probed via a study of the quark-antiquark-gluon fluctuations of the incoming photon [35]. The fit of Ref. [31] suggests that the shapes of the  $\beta$ -distributions of the diffractive gluon and quark densities at low  $Q^2$ ,  $Q^2 \sim 4 \text{ GeV}^2$ , are similar. This leads to the similar coherence lengths  $l_c^{eff}$  (up to the effects related to the region of small  $\beta$ , which are somewhat different in the two cases). With an increase of  $Q^2$ , larger scaling violations in the gluon channel lead to a faster decrease with  $Q^2$  of  $l_c^{eff}$  for the gluon channel than for the quark channel. The detailed  $Q^2$  dependence of  $l_c^{eff}$  for the gluon channel will be presented elsewhere.

### C. The dynamics of compact systems

As discussed in the Introduction, at high energy, a projectile consists of coherent quark-gluons configurations of very different transverse spatial sizes. One can select rare processes where the small-size, or compact, quark-gluon fluctuations either dominate the process as in electroproduction of vector mesons by longitudinally polarized photons with high  $Q^2$  or are as important as the large-size configurations as in inclusive DIS or in diffractive processes initiated by transversely polarized photons. The cross section of the interaction of the small-size configuration with the hadronic target is calculable in pQCD since small distances correspond to large  $Q^2$ , where pQCD is applicable. It was found that the small-size configurations have reduced interactions with the target.

The cross section of the interaction of a compact  $q\bar{q}$  fluctuation of the virtual photon with

a hadronic target  $T$  was derived in the leading  $\alpha_s \log(Q^2/\Lambda^2)$  approximation in [7,22,36,37]<sup>3</sup>

$$\sigma_T^{q\bar{q}}(b^2, x) = \frac{\pi^2}{3} b^2 \left[ x G_T(x, \lambda/b^2) \right] \alpha_s(\lambda/b^2), \quad (13)$$

where  $b = (b_q - b_{\bar{q}})$  is the transverse inter-quark distance within the wave function of the photon;  $\alpha_s(\lambda/b^2)$  is the QCD coupling constant;  $G_T(x, \lambda/b^2)$  is the gluon parton density of the target. This formula is a consequence of gauge invariance, asymptotic freedom, and the factorization theorem in QCD. The QCD evolution is properly taken into account through the gluon distribution of the target  $G_T(x, Q_{eff} = \lambda/b^2)$ . The scale factor  $\lambda$  can be estimated from the analysis of the  $\sigma_L(\gamma^* N)$  cross section [7].  $\lambda$  slowly increases with the decrease of  $x$  due to the increase of the gluon density at small  $x$ . For  $x \sim 10^{-3}$  and  $Q^2 \approx 10$  GeV $^2$ ,  $\lambda \approx 10$ . For a recent detailed study of an approach to inclusive DIS based on Eq. (13), see [38].

For a colorless dipole consisting of two gluons, the dipole cross section will be larger by a factor of 9/4, which is the ratio of the Casimir operators of the SU(3)<sub>c</sub> color group for the octet and triplet representations [2]. Note that this observation is consistent with the analysis of DIS data in Ref. [27] which demonstrated that the effective dipole cross section in the gluon channel is larger (by approximately a factor of 3) than in the quark channel.

The gluon density of the target in Eq. (13) is a feature that is absent in the two-gluon exchange models [39]. The two-gluon description in [39] is incomplete because at small Bjorken  $x$ , a compact quark-gluon configuration interacts with the target by producing a soft self-interacting multi-gluon field. The effect of this soft gluon field is expressed by the gluon parton density of the target  $x G_T(x, \lambda/b^2)$ .

The proportionality of  $\sigma_T^{q\bar{q}}(b^2, x)$  to the gluon density  $x G_T(x, \lambda/b^2)$  has found many experimental confirmations in inclusive DIS and in hard exclusive reactions on nucleon and nuclear targets.

Let us consider the implications of Eq. (13) for inclusive DIS scattering and for the famous approximate Bjorken scaling for the total photoabsorption cross section  $\sigma_{tot}(\gamma^* + p \rightarrow X)(Q^2, x)$ . According to Eq. (13), the cross section for the interaction of a compact quark-gluon configurations with a target is proportional to the transverse size  $b^2 \propto 1/Q^2$  of the compact configuration. It is important to note that this non-trivial result contradicts our experience from the models, which existed before QCD. For example, in the meson cloud models of the photon wave function, all meson configurations interact with the target with typical hadron-nucleon (nucleus) cross sections. In the case of DIS on nuclei at not extremely small  $x$ , such a behaviour leads to  $\sigma_{tot} \propto \ln x$  at  $x \ll 1/2R_A m_N$  (see Eq. (2)), which contradicts the experimentally observed Bjorken scaling and causes a paradox. The paradox is known as the Gribov paradox.

QCD explains the origin of the Gribov paradox. Indeed, in pQCD, the contribution of small-size configurations to  $\sigma_{tot}(\gamma^* + p \rightarrow X)(Q^2, x)$  behaves as  $1/Q^2$  according to Eq. (13). As a result, it has the same  $Q^2$  dependence as the non-perturbative contribution of large-size configurations to  $\sigma_{tot}(\gamma^* + p \rightarrow X)(Q^2, x)$ , which is suppressed by a factor proportional to  $1/Q^2$  since the large-size configurations occupy a small fraction  $\sim k_t^2/Q^2$  of the phase

<sup>3</sup>This formula is also valid in the leading  $\alpha_s \log x$  approximation.

volume. Therefore, the sum of these two contributions behaves approximately as  $1/Q^2$  at large  $Q^2$  in accordance with the approximate Bjorken scaling.

The QCD prediction of Eq. (13) and its experimental confirmation both demonstrate that the existence of quark-gluon configurations, interacting weakly with hadron targets, is a fundamental property of QCD.

Eq. (13) substantiates the pre-QCD hypothesis of J. Bjorken, which became known as the aligned jet model [40]. Within the framework of the parton model, Bjorken offered a solution of the Gribov paradox by suggesting that the interaction of the quark and anti-quark with large relative transverse momenta  $p_t$ , which form the photon wave function, with hadronic targets is suppressed by some factor  $f(\mu^2/(p_t^2 + \mu^2))$ , where  $\mu$  is a cut-off scale. Since large relative momenta correspond to small relative distances, the aligned jet model foresaw the suppression of the interaction of the spatially small quark-antiquark dipole. So, in the aligned jet model, only large-size configurations take part in the interaction with the target. Since the available phase space of the aligned jet configurations is proportional to  $1/Q^2$ , the scaling of  $\sigma_{tot}(\gamma^* + p \rightarrow X)(Q^2, x)$  is restored in the aligned jet model.

In QCD, Bjorken's aligned jet model needs to be modified. Firstly, Bjorken scaling of  $\sigma_{tot}(\gamma^* + p \rightarrow X)(Q^2, x)$  is only approximate due to the QCD evolution with  $\log(Q^2)$  of parton densities of the target. Secondly, as one can see from Eq. (13), the interaction of small configurations is suppressed but not negligible. Thirdly, as a result of the QCD evolution, the gluon parton density of the target becomes large at small  $x$ , which makes the cross section sizable even for relatively small  $b$ . Fourthly, one has to account for the suppression of on-mass-shell quark production and for the compensation of this suppression by the radiation of hard gluons ( see, e.g., [17,41]).

Leading twist nuclear shadowing predicted by the QCD-improved aligned jet model has been observed in inclusive DIS scattering on light and heavy nuclei, see [15,16] and references therein.

#### D. The factorization theorem for hard exclusive meson electroproduction off hadronic targets

A crucial element of perturbative calculations in QCD are factorization theorems. Such theorems prove that amplitudes of certain hard processes can be computed as the convolution of the hard part, which can be computed in pQCD, and of the soft, non-perturbative, part, which contains information about parton distributions in the target.

Recently J. Collins *et al.* [5] have proved the QCD factorization theorem for hard exclusive meson production in the reaction  $\gamma_L^* + T \rightarrow M + T'$ , where  $M$  is a meson ( $\rho, \pi, K, \eta, \dots$ ) and  $T$  and  $T'$  are baryon states of a fixed mass. This theorem is valid for hard processes initiated by a highly virtual longitudinally polarized photon on any hadron target at fixed  $x$  and  $Q^2 \gg \Lambda_{QCD}^2$ . The amplitudes of such processes are calculable as the convolution of the hard kernel  $H_{ij}(Q^2 x_1/x, Q^2, z, \mu^2)$ , calculable in pQCD for a given minimal Fock component of the light-cone wave function of the meson wave function  $\phi_j^M(z, \mu^2)$ , and the skewed parton densities of the target  $f_{i/p}(x_1, x_1 - x, t, \mu^2)$  (see Fig. 4 for the schematic representation of the amplitude for the process  $\gamma_L^* + T \rightarrow M + T'$ )

$$A = \sum_{i,j} \int_0^1 dz \int dx_1 f_{i/p}(x_1, x_1 - x, t, \mu^2) H_{ij}(Q^2 x_1/x, Q^2, z, \mu^2) \phi_j^M(z, \mu^2). \quad (14)$$

In Eq. (14),  $z$  is the fraction of the photon longitudinal momentum, carried by the quark or antiquark that constitutes the meson  $M$ ;  $\mu^2$  is the factorization scale which is usually set to  $Q^2$ ;  $x_1$  and  $x_1 - x$  are the longitudinal light-cone momentum fractions of the partons connecting the hard and soft parts of the amplitude  $A$ . Note that the skewed parton densities evolve as a function of  $x_1$  and  $Q^2$  for fixed  $x = Q^2/2(p \cdot q)$ , while the conventional parton densities evolve as a function of  $x$  and  $Q^2$ . In order to emphasize this difference, we keep a different notation for the skewedness parameter  $\Delta \equiv x_1 - (x_1 - x) = x$ .

A similar QCD factorization theorem can be derived if  $M$  and  $T$  are baryons and  $T'$  is a meson.

Applications of the factorization theorem give a practical possibility of calculating cross sections of hard exclusive processes in the same sense as total cross sections of inclusive DIS [5–7]. The kernels for the QCD evolution of the skewed (nondiagonal, nonforward) parton densities have been calculated in the leading  $\alpha_s \log(Q^2/\Lambda^2)$  approximation in [42,43] and in the next-to-leading  $\alpha_s \log(Q^2/\Lambda^2)$  approximation in [44,45]. Thus, the major difference between computing cross sections of hard diffractive processes and more familiar inclusive DIS processes consists in the necessity to use the skewed parton densities instead of the conventional parton densities.

A natural assumption for the input skewed parton densities  $f_{i/p}(x_1, x_1 - x, t, \mu^2)$  at the initial scale  $\mu = Q_0$  of the QCD evolution and small  $x$  is that they should be taken equal to the usual parton densities at  $Q_0$  [43]. This conjecture is based on the observation that the effect of skewedness (nondiagonality) should be negligible at large  $x_1$  and small  $Q_0$  from which the QCD evolution starts, i.e. one can neglect the effect of  $\Delta$  at the input scale  $Q_0$ . We refer the reader to Subsec. IV A where this question is investigated in detail by analyzing general tendencies of the QCD evolution in the  $x - Q$ -plane.

Practical ways to estimate skewed parton densities through conventional parton densities were suggested in Ref. [43,46]. In particular, using symmetries of the kernels of the skewed QCD evolution, it was proposed in Ref. [2,46] that the skewed parton densities at given  $x_1$  and  $x$  are expressed through the conventional parton densities computed at smaller  $x' = x_1 - \Delta/2$ . The numerical analysis of [47] showed that, indeed, it is more appropriate to compare the skewed parton densities to the usual parton densities taken at  $x' < x_1$ .

The factorization theorem for hard exclusive meson electroproduction off nucleon or nuclear targets enables one to experimentally measure the skewed parton distributions in the nucleon (nucleus) and the distribution of bare quarks within mesons and nucleons (the minimal Fock components in the wave functions of mesons and nucleons). The number of the skewed parton distributions is much larger than the number of parton distributions measured in inclusive DIS since the former includes, for example, transitions like  $N \rightarrow \Lambda$ , various distributions of spin, etc. Thus, it is reasonable to expect significant progress in the understanding of the structure of baryons and mesons from the investigation of hard diffractive processes.

### III. HARD DIFFRACTIVE PROCESSES

In this section, we discuss the implications of color coherence for hard diffractive processes on nucleons and nuclei.

#### A. The phenomenon of Generalized Color Transparency

The phenomenon of the complete disappearance of initial and final state interactions of spatially small-size wave packets of quarks and gluons, produced in hard exclusive processes, is usually referred to as the phenomenon of color transparency. Initial theoretical ideas on the color transparency phenomenon were intuitive and based on model assumptions. For the history of the development of this subject and appropriate references, see, e.g., [1]. The recent progress in the theoretical understanding of the color transparency phenomenon is based on the systematic application of the QCD factorization theorem to hard exclusive and semi-exclusive reactions. In particular, the application of the factorization theorem to hard diffractive vector meson  $V$  production on nuclear and nucleon targets at sufficiently small  $x$  enables one to express the ratio of the forward differential cross sections for the nucleus and the nucleon as (compare to Eq. (14))

$$\frac{d\sigma^{\gamma^*+A \rightarrow V+A}/dt(t=0)}{d\sigma^{\gamma^*+N \rightarrow V+N}/dt(t=0)} = \frac{\sum_{i,j} \int_0^1 dz \int dx_1 f_{i/A}(x_1, x_1 - x, t=0, Q^2) H_{ij}(Q^2 x_1/x, Q^2, z) \phi_j^V(z, Q^2)}{\sum_{i,j} \int_0^1 dz \int dx_1 f_{i/N}(x_1, x_1 - x, t=0, Q^2) H_{ij}(Q^2 x_1/x, Q^2, z) \phi_j^V(z, Q^2)}, \quad (15)$$

where  $f_{i/A}(x_1, x_1 - x, t, Q^2)$  is the nuclear skewed parton density of parton  $i$ .

The phenomenon, described by Eq. (15), can be called generalized color transparency [3,4,21]. Although it resembles color transparency, the two phenomena lead to qualitatively different patterns of  $A$  dependence for sufficiently small  $x$ . Indeed, in case of the color transparency phenomenon, the complete disappearance of the initial and final state interactions of the  $q\bar{q}$  pair, when  $x$  decreases, is predicted [48]. On the contrary, in the case of the generalized color transparency phenomenon, the initial state interactions with nuclear medium do not disappear but increase with a decrease of  $x$ . They are included into nuclear modifications of parton distributions (nuclear shadowing of parton distributions) the nuclear target  $f_{i/A}(x_1, x_1 - x, t, Q^2)$  (see, e.g., Fig. 5).

It is important to repeat that the considered example of diffractive production of vector mesons presents a particular case of the QCD factorization theorem which states that nuclear effects in hard exclusive processes at small  $x$  are calculable in QCD within the framework of the generalized (skewed) QCD evolution equation for the parton distributions of nuclei.

Now let us consider two limiting cases of Eq. (15). In the limit of fixed  $x$  and  $Q^2 \rightarrow \infty$ , the nuclear effects in the parton distributions disappear, i.e.  $f_{i/A}(x_1, x_1 - x, t, Q^2) \rightarrow A f_{i/N}(x_1, x_1 - x, t, Q^2)$ . This leads to the more familiar phenomenon of color transparency

$$\frac{d\sigma^{\gamma^*+A \rightarrow V+A}/dt(t=0)}{d\sigma^{\gamma^*+N \rightarrow V+N}/dt(t=0)} = A^2. \quad (16)$$

Eq. (16) is a consequence of the disappearance of nuclear effects in the skewed nuclear parton densities as a result of the QCD evolution. The reason for such a disappearance is that the skewed (as well as conventional) parton densities at given  $x$  and  $Q^2$  are determined by the input parton distributions at significantly larger  $x$  and smaller  $Q_0^2$  where nuclear shadowing is unimportant. Thus, as one evolves from  $Q_0^2$  to  $Q^2$ , the unshadowed large- $x$  region contributes at smaller  $x$  and, consequently, diminishes the effect of shadowing. It explains how color transparency takes over generalized color transparency in the limit of fixed  $x$  and  $Q^2 \rightarrow \infty$ . We also refer the reader to Subsec. IV A, where general trends of the QCD evolution in the  $x - Q$ -plane are discussed on the quantitative level.

In order to illustrate the onset of color transparency numerically, we perform an analysis of the QCD evolution of the skewed and conventional nuclear parton densities. Details of the analysis are presented in Subsect. IV B. The limiting case, when  $x$  is fixed and  $Q^2 \rightarrow \infty$ , is presented in Figs. 6 and 7. One can see that, at  $x = 10^{-3}$  and large  $Q^2$ , the ratio of nuclear to nucleon skewed and conventional gluon parton densities increases and will eventually approach unity. This observation implies that the effect of nuclear shadowing vanishes and Eq. (16) is justified in the discussed limit.

In the other limit of fixed  $Q^2$  and  $x \rightarrow 0$ , QCD predicts that nuclear effects begin to play an important role. This occurs due to the growing importance of nuclear shadowing at small  $x$ . This effect can also be interpreted as the decrease of the influence of color transparency. This limiting case for the conventional gluon parton densities is presented in Fig. 8. The ratio of the nuclear to nucleon conventional gluon parton densities becomes smaller at fixed  $Q^2$  and  $x \rightarrow 0$ , which demonstrates the increase of nuclear shadowing.

Within the models, inspired by the two-gluon exchange model [39], i.e. by the analysis of the lowest-order diagrams of pQCD (see Ref. [48], for example), shadowing for the interaction of small dipoles is a higher twist effect which decreases  $\propto 1/Q^2$  when  $Q^2$  increases. The difference between the predictions of [48] and our analysis is due to the lack of Gribov diffusion to larger size configurations in the parton ladder in the lowest-order Feynman diagrams [10,11]. Gribov diffusion has been observed long ago as a shrinkage of the diffractive peak in  $p\bar{p}$  collisions with increasing energy. Another cause for the difference is that the QCD evolution equation predicts increasing parton densities at small  $x$ . This feature is also absent in the lowest-order Feynman diagrams.

## B. A brief review of experimental data

The current subsection is concerned with hard exclusive reactions in the kinematic limit where color transparency plays a dominant role. Namely, these reactions are vector meson electroproduction off nuclear targets, coherent photoproduction of  $J/\psi$ , pion diffractive dijet production on nuclei and processes where the two-gluon exchange is prohibited.

Exclusive meson production by longitudinal photons was discussed in the previous subsection. Eq. (15) represents the ratio of the corresponding forward differential cross sections. In the limit of fixed small  $x$  and  $Q^2 \rightarrow \infty$ , Eq. (15) has been proven in QCD within the leading  $\alpha_s \log(Q^2/\Lambda^2) \log x$  approximation in [21] and within the leading  $\alpha_s \log(Q^2/\Lambda^2)$  approximations in [7].

Originally, in [7,21], Eq. (15) was obtained using the conventional gluon parton densities. The factorization theorem for exclusive vector meson electroproduction requires that the

skewed parton densities are used instead of the conventional parton densities. However, regardless of whether skewed or conventional parton densities of the target are used, Eq. (15) leads to Eq. (16) because in the limit of fixed small  $x$  and  $Q^2 \rightarrow \infty$  nuclear shadowing disappears in both skewed and conventional parton densities, as we explained in Subsec. III A.

An additional  $A$  dependence of the cross section for exclusive vector meson electro-production is also present. The cross section is proportional to the square of the nuclear form factor  $F_A^2(t_{min}) = \exp(-m_N^2 x_{Bj}^2 R_A^2/3)$ , where  $-t_{min} = m_N^2 x_{Bj}^2$  is the minimal momentum transfer to the target. However, due to the smallness of  $x_{Bj}$  considered here,  $x_{Bj} \ll \sqrt{3}/(R_A m_N) \approx 0.34/A^{1/3}$ , the effect of the nuclear form factor is negligible in Eqs. (15) and (16).

The behaviour, predicted by Eq. (15), has been verified experimentally in a number of phenomena. The E665 data on exclusive  $\rho$  meson electroproduction off nuclear targets [49] reveals that the  $A$  dependence of the cross section increases with the increase of  $Q^2$ . Such a behaviour is a characteristic feature of the color transparency phenomenon. However, this result should be considered with a grain of salt because part of the  $Q^2$  dependence can be attributed to the fact that in the kinematics, covered by the E665 data, the coherence length  $l_c$  is comparable with the nuclear radius and that within the data sample  $l_c$  depends on  $Q^2$ .

Another example of processes, where color coherence plays a principal role, is coherent photoproduction of  $J/\psi$ . The data on the cross section of coherent photoproduction of  $J/\psi$  off nuclei [50] at  $\langle E_\gamma \rangle = 120$  GeV and  $x_{eff} \approx 0.04$ , where the shadowing effects in the gluon density are negligible, demonstrates that the cross section is proportional to  $A^n$  with  $n \approx 1.4 \pm 0.06 \pm 0.04$ . This result is consistent with the idea in [51] that  $J/\psi$ , produced in exclusive photoproduction processes, originates from conversion of the photon to a  $c\bar{c}$  quark pair at small relative distances, which hence interacts with a small interaction cross section. At the same time, the genuine  $J/\psi$ -nucleon cross section could be significantly larger because, in case of  $J/\psi$ -nucleon interaction, the  $c\bar{c}$  quarks are at average distances within  $J/\psi$  [51,52].

Hard diffractive electroproduction of vector mesons, described above, is dominated by small-size quark-gluon configurations, enforced by choosing the special kinematic condition of  $Q^2 \rightarrow \infty$ . This condition selects small transverse size  $q\bar{q}$  configurations in longitudinal photons. Another way to select small transverse size configurations, is to choose a special final state. An example of such a process is coherent diffractive production of mini-jets by pions in the reaction  $\pi + A \rightarrow jet(k_t) + jet(-k_t) + A$ . If we impose the restriction that only high transverse momentum  $k_t$  jets are produced and that only the diffractive peak is investigated such that the nucleus  $A$  is intact, then it would insure only small  $q\bar{q}$  configurations in the wave function of the incoming pions.

The recent Fermilab experiment E791 data on diffractive dijet production by a pion projectile with momentum of 500 GeV/c off nuclear targets of carbon and platinum [53] is consistent with the predictions of the generalized color transparency [22]. The analysis of the E791 data demonstrates that  $\sigma(\pi + A \rightarrow 2jets + A) \propto A^{1.61 \pm 0.08}$  for  $1.5 \text{ GeV/c} < k_t < 2.0 \text{ GeV/c}$  and  $\sigma \propto A^{1.65 \pm 0.09}$  for  $2.0 \text{ GeV/c} < k_t$  [23]. These results are consistent with the predictions based on color transparency.

It is important to stress that this  $A$  dependence is significantly faster than the expected  $A$  dependence for usual soft diffraction discussed in Sect. V. Namely, the ratio of the cross

sections for platinum and carbon,  $\sigma_{Pt}/\sigma_C$  observed in the E791 experiment, is approximately seven times larger than this ratio, estimated within the framework of soft diffraction, where  $\sigma \propto A^{2/3}$ .

In addition to the  $A$  dependence, the E791 experiment confirmed other expectations for the color transparency regime: i) The pion wave function at  $Q^2 \approx 10 \text{ GeV}^2$  ( $k_t > 1.5 \text{ GeV}/c$ ) is described well by the asymptotic wave function calculable in pQCD,  $|\Psi_\pi(z)|^2 \propto z^2(1-z)^2$ , where  $z$  is the fraction of the longitudinal momentum of the pion carried by a quark in the infinite momentum frame [54,55]; ii) The  $k_t$  dependence of the cross section at  $k_t > 1.5 \text{ GeV}/c$  is also consistent with the pQCD calculation of [22].

It is important to note that the observed  $A$  dependence of the cross section of diffractive dijet production is close to that found for exclusive photoproduction of  $J/\psi$  [50]. This observation is in line with the QCD factorization theorem of [5] since the cross sections for diffractive dijet production and exclusive photoproduction of  $J/\psi$  are expressed through the same nuclear skewed gluon distribution at similar light-cone gluon momenta.

More experiments are needed to understand the dynamics of hard diffractive exclusive processes more clearly. We suggest measuring diffractive dijet production off nuclei by different projectiles, such as kaons, or to measure charmed jet production by real photons.

Eqs. (15) and (16) are very general. They have been proven using the QCD factorization theorem and the QCD evolution equation. According to the QCD factorization theorem for certain hard processes dominated by the scattering of compact system from hadron (nuclear) targets, the cross sections are expressed through the target parton (gluon) densities. But, as it follows from the QCD evolution equation, nuclear shadowing vanishes at fixed  $x$  with the increase of  $Q^2$ . Hence, in this limit, Eq. (16) is justified. A similar prediction is also applicable to the processes where the exchange with vacuum quantum numbers in  $t$  channel is forbidden and where as a result the two-gluon exchange does not contribute. Below we will give a few examples of such processes.

The QCD factorization theorem predicts the color transparency phenomenon for the zero-angle charge-exchange coherent processes, initiated by longitudinal photons in the limit of  $Q^2 \rightarrow \infty$  and  $1/(2m_N x) \gg R_A$  (so that the effect of  $t_{min}$  in the nuclear form factor is small) but  $l_c^{eff} \ll r_{NN}$ , where  $r_{NN}$  is the average internucleon distance in the nucleus [3]

$$\frac{d\sigma(\gamma_L^* + A \rightarrow \rho^- + A')/dt}{d\sigma(\gamma_L^* + B \rightarrow \rho^- + B')/dt} = \frac{|\langle A|T_+|A' \rangle|^2}{|\langle B|T_+|B' \rangle|^2}, \quad (17)$$

where  $A'$  ( $B'$ ) is the isobaric state of a nucleus with the atomic number  $A$  ( $B$ ) with a neutron substituted by a proton;  $T_+$  is the isospin-raising operator.

In order to diminish the sensitivity of the discussed processes to the nuclear wave function of the isobaric states, it can be compared with the zero-angle charge-exchange coherent processes initiated by high-energy neutrinos or anti-neutrinos:

$$\frac{d\sigma(\nu_l + A \rightarrow l + A')/dt}{d\sigma(\nu_l + B \rightarrow l + B')/dt} = \frac{|\langle A|T_+|A' \rangle|^2}{|\langle B|T_+|B' \rangle|^2}, \quad (18)$$

where  $\nu_l$  is the neutrino corresponding to the lepton  $l$ .

Another example of zero-angle charge-exchange coherent processes, where color transparency dominates, is the production of electrically charged pseudo-scalar mesons [3]. In

the limit of  $Q^2 \rightarrow \infty$  and  $l_c \geq R_A$  but  $l_c^{eff} \ll r_{NN}$ , QCD predicts for the reactions, initiated by virtual photons

$$\frac{d\sigma(\gamma_L^* + A \rightarrow \pi^- + A')/dt}{d\sigma(\gamma_L^* + B \rightarrow \pi^- + B')/dt} = \frac{|\langle A|T_+|A'\rangle|^2}{|\langle B|T_+|B'\rangle|^2}. \quad (19)$$

It is important to emphasize that in the processes, described by Eqs. (17), (18), and (19), exchange by quarks is required.

Similar predictions are applicable for the coherent production of  $\pi^+$ ,  $\rho^+$  and  $f$  mesons and pairs of mesons.

The QCD factorization theorem [5] can be generalized to semi-inclusive processes off nuclei with large rapidity gap between the photon and target fragmentation regions. For zero-angle scattering, at  $Q^2 \rightarrow \infty$  and fixed  $x$ , the onset of color transparency is expected

$$\frac{d}{dt}\sigma(\gamma_L^* + A \rightarrow M + Rap. Gap + X') = A \frac{d}{dt}\sigma(\gamma_L^* + N \rightarrow M + Rap. Gap + X'). \quad (20)$$

It is necessary to stress that in practical applications taking account of the leading twist effects in Eqs. (15), (16), and (20) is insufficient since the small transverse size wave packet produced tends to expand to a normal hadronic size. In order to suppress this effect, one needs to impose the specific kinematic conditions – rather large  $Q^2$  or sufficiently small  $x$  – so that the expansion will happen outside of the nucleus.

### C. Hard diffractive processes at HERA

In this subsection, experimental results, obtained at HERA, are reviewed from the point of view of color coherence.

Hard diffractive electroproduction of vector mesons on hydrogen  $\gamma^* + p \rightarrow V + p$ , where  $V = \rho$ ,  $\phi$ , or  $J/\Psi$ , has recently been observed at HERA [14]. The data shows several phenomena, expected in QCD. Firstly, QCD predicts the increase of the cross section of hard diffractive processes, initiated by a projectile in a spatially small configuration of the size  $1/Q^2$ , as a power of the invariant energy of the collision<sup>4</sup>

$$\sigma(\text{hard diffractive}) \approx (xG_p(x, Q^2))^2. \quad (21)$$

Such a behaviour has been proven within the leading  $\alpha_s \log x$  approximation in [21,56] and within the leading  $\alpha_s \ln Q^2 / \Lambda^2$  approximation in [5,7,22]. The result of Eq. (21) is in broad agreement with the energy dependence of cross sections for diffractive electroproduction of vector mesons  $\rho$ ,  $\phi$ , and  $J/\psi$  observed at HERA [14]. The rapid increase of the cross sections of hard diffractive processes with increasing energy is one of the signatures of the color transparency phenomenon [21].

<sup>4</sup>Of course, one should use skewed parton densities in Eq. (21). However, in the kinematics of the experiments, the numerical difference between the skewed and conventional parton densities is rather small.

Secondly, the data have confirmed other QCD predictions for hard exclusive diffractive electroproduction of vector mesons such as the enhancement of heavy flavor vector mesons production (in contrast to moderate  $Q^2$  processes, in which production of heavy flavors is suppressed), dominance of the longitudinal over transverse cross sections at large  $Q^2$ , the universal dependence of cross sections of hard diffractive processes on the momentum transfer  $t$ , large cross sections of diffractive production of excited states of vector mesons, restoration of the SU(3) symmetry prediction for the ratio of cross sections for different vector mesons in the final state, etc. For the review and references see [1,2,14]. The current data is consistent with the expectation of the onset of the hard QCD regime for hard diffractive processes at large  $Q^2$  [14]. Hence, the discovery of a variety of new calculable in QCD hard phenomena is expected.

An important remark here is in order. All the above discussed hard exclusive diffractive processes were initiated by longitudinal photons. In such processes, the hardness of the photons (when the photons have large  $Q^2$ ) leads to color transparency. This logic is inapplicable to the processes, dominated by transversely polarized photons. In case of transverse photons, the soft component of the wave function (large size) may be as important as the hard component (small size). However, as a result of the Sudakov-type form factors, contributions of the soft component are suppressed at very large  $Q^2$ . The relative importance of small and large dipole sizes in exclusive diffraction, initiated by transversely polarized photons, requires further studies.

The importance of the soft component of the transversely polarized virtual photons manifests itself in the discovery of significant cross sections of diffraction in DIS [14] and in the leading twist nuclear shadowing in DIS [15,16]. For these processes, the hardness does not necessarily mean color transparency. The recent data of HERA [14] suggests that, for  $Q^2 \geq 6 \text{ GeV}^2$ , exclusive electroproduction of vector mesons is dominated by the compact configuration of the photon wave function. If so, generalized color transparency will be applicable to coherent diffractive electroproduction of transversely polarized vector mesons at these  $Q^2$ .

#### D. Hard diffractive electroproduction of photons

The generalized vector dominance model (GVMD) is often considered as an alternative to the QCD explanation of the inclusive and diffractive DIS, for a recent review and references see [57]. In the GVMD model, using the basis of hadronic states, the (virtual) photon interaction with the nucleon proceeds via the transition of the photon into different vector meson states, when the diagonal  $V + N \rightarrow V + N$  and non-diagonal  $V + N \rightarrow V' + N$  transitions are accounted for.

It was argued in [58] that the GVMD models are successful in the theoretical description of photoproduction and electroproduction at high energies since they possess (in an approximate way) basic features of theories with color coherence.

However, it turns out that the process of diffractive electroproduction of photons in the DIS reaction  $\gamma^*(Q^2) + p \rightarrow \gamma^*(Q_f^2) + p'$ , which has been a subject of recent theoretical and experimental studies, can discriminate between the GVMD and pQCD pictures of DIS. Within the framework of pQCD, the ratio of the imaginary parts of the amplitudes of the

real and virtual photon electroproduction was found to be approximately independent of  $Q^2$  at small  $x$  [59]

$$\frac{\text{Im}A(\gamma^*(Q^2) + p \rightarrow \gamma(Q^2 = 0) + p')}{\text{Im}A(\gamma^*(Q^2) + p \rightarrow \gamma^*(Q^2) + p)} \approx 2. \quad (22)$$

The recent HERA data [60] seems to confirm the result of Eq. (22).

Within the framework of the GVMD model, which contains non-diagonal transition between the neighbouring vector mesons [61], it was found in [58] that

$$\begin{aligned} & \frac{\text{Im}A(\gamma^*(Q^2) + p \rightarrow \gamma(Q^2 = 0) + p')}{\text{Im}A(\gamma^*(Q^2) + p \rightarrow \gamma^*(Q^2) + p)} = \\ & \left( \sum_{nm} \frac{e}{f_n} \frac{M_n^2}{M_n^2 + Q^2} \Sigma_{nm} \frac{e}{f_m} \right) / \left( \sum_{nm} \frac{e}{f_n} \frac{M_n^2}{M_n^2 + Q^2} \Sigma_{nm} \frac{e}{f_m} \frac{M_m^2}{M_m^2 + Q^2} \right). \end{aligned} \quad (23)$$

The comparison of predictions of Eqs. (22) and (23) is presented in Fig. 9. One can readily see that the result of the GVMD model is consistent with the pQCD result only in a limited range of  $Q^2$ ,  $1 \leq Q^2 \leq 5 \div 6 \text{ GeV}^2$ . Hence, the forthcoming HERA data on diffractive electroproduction of photons in the DIS reaction  $\gamma^*(Q^2) + p \rightarrow \gamma^*(Q_f^2) + p'$  in a wide range of  $Q^2$ , would allow to establish the limits of applicability of the complementary description of DIS, which employs the GVMD models with elements of color transparency built-in.

#### IV. NUMERICAL ANALYSIS OF THE DGLAP QCD EVOLUTION

In this section, the onset of color transparency and generalized color transparency is studied numerically by performing the QCD evolution of parton densities of nuclei. Adopting a reasonable algorithm, we also analyze the paths in the  $x - Q$ -plane along which the QCD evolution proceeds. The knowledge of these paths enables one to substantiate the choice of the initial condition for the QCD evolution of the skewed parton densities and to explain the  $Q^2$  evolution of nuclear parton densities. Also, the limits of applicability of the QCD evolution for nuclear parton densities are estimated.

##### A. The QCD evolution paths

The integro-differential DGLAP evolution equations, which govern the  $Q^2$  and  $x$  dependence of parton densities, read as follows

$$\begin{aligned} \frac{dq^{NS}(x, Q^2)}{d\ln Q^2} &= \frac{\alpha_s(Q^2)}{2\pi} \int_x^1 \frac{dy}{y} q^{NS}(y, Q^2) P_{qq}\left(\frac{x}{y}\right), \\ \frac{d}{d\ln Q^2} \begin{pmatrix} q^S(x, Q^2) \\ g(x, Q^2) \end{pmatrix} &= \frac{\alpha_s(Q^2)}{2\pi} \int_x^1 \frac{dy}{y} \begin{pmatrix} P_{qq}\left(\frac{x}{y}\right) & P_{qg}\left(\frac{x}{y}\right) \\ P_{gq}\left(\frac{x}{y}\right) & P_{gg}\left(\frac{x}{y}\right) \end{pmatrix} \begin{pmatrix} q^S(y, Q^2) \\ g(y, Q^2) \end{pmatrix}. \end{aligned} \quad (24)$$

In Eqs. (24),  $q^{NS}(x, Q^2) = q_i(x, Q^2) - q_j(x, Q^2)$ , with any  $i \neq j$ , is the quark flavor non-singlet distribution;  $q^S(x, Q^2) = \sum_i (q_i(x, Q^2) + \bar{q}_i(x, Q^2))$  is the quark flavor singlet distribution;  $g(x, Q^2)$  is the gluon distribution;  $\alpha_s(Q^2)$  is the running QCD coupling constant;  $P_{qq}(x/y)$ ,  $P_{qg}(x/y)$ ,  $P_{gq}(x/y)$ , and  $P_{gg}(x/y)$  are the splitting functions calculable in pQCD.

Eqs. (24) are often solved numerically. One example is the brute force method, when iterations in  $Q^2$  are used. In particular, knowing the parton densities at  $Q_0^2$ , one can find the parton densities at larger  $Q^2$  using Eq. (24) as

$$q^{NS}(x, Q^2) = q^{NS}(x, Q_0^2) + \frac{Q^2 - Q_0^2}{Q_0^2} \frac{\alpha_s(Q_0^2)}{2\pi} \int_x^1 \frac{dy}{y} q^{NS}(y, Q_0^2) P_{qq}\left(\frac{x}{y}\right). \quad (25)$$

Similarly, Eq. (24) can be solved for the quark flavor singlet and gluon parton densities. By choosing the difference between  $Q^2$  and  $Q_0^2$  small enough and repeating the procedure of Eq. (25) a desired number of times, each time using the parton densities from the previous step in  $Q^2$ , one finds the solution of Eq. (24). From Eq. (25) one can see that the parton densities at the input scale  $Q_0^2$  determine the the parton densities at a larger scale  $Q^2$ ,  $Q^2 > Q_0^2$ .

The general trends of the QCD DGLAP  $Q^2$  evolution are well known. As  $Q$  increases, the parton densities shift toward lower  $x$  due to the emission of soft partons. So, the QCD evolution proceeds along a path in the  $x - Q$ -plane, which extends from low  $Q$  and high  $x$  towards large  $Q$  and small  $x$ . The detailed knowledge of this path is very important. It enables one, for example, to estimate the influence of the input parton densities at the initial scale  $Q_0$  on the result of the QCD evolution at higher  $Q$  and judge which regions of  $x$  at  $Q_0$  contribute to the parton densities at  $Q > Q_0$ . Thus, our study of the general trends of the QCD evolution addresses the issues of the choice of the input distribution for the QCD evolution for the skewed parton densities and the  $Q^2$  and  $x$  dependence of nuclear shadowing. It might also contribute to our understanding of the limits of applicability of the leading twist QCD evolution equation.

In order to investigate a path in the  $x - Q$ -plane relevant for the QCD evolution, the following algorithm was adopted.

- Fix the final point of the QCD evolution at some large  $Q$  and small  $x$ . We have studied three different final points at  $Q=5$  GeV and  $x=10^{-4}$ ,  $10^{-3}$ , and  $10^{-2}$ . By solving Eq. (25) numerically, we find the parton densities at these final points.
- Begin increasing the lower limit of integration in Eq. (25) from  $x$  to some  $x'$ . It will decrease the integration interval over  $y$  at the initial scale  $Q_0$ , which contributes to the parton densities at the final points – the values of the parton densities at the final points will decrease. Choose  $x'$  such that the integration from  $x'$  to 1 in Eq. (25) gives the parton densities at the final points, which are half the parton densities, when the integration takes place from  $x$  to 1. Then, for each final point, i.e. for each pair  $(Q > Q_0, x)$ ,  $x'$  represents the average  $x$  at  $Q_0$ . Take those  $x'$  as the initial point of the QCD path.
- Now that the initial and final points of the path are known, one needs to connect them, i.e. one needs to find pairs  $(Q_0 < Q < 5 \text{ GeV}, x'')$  through which the path passes. At each  $Q_0 < Q < 5 \text{ GeV}$ ,  $x''$  is found by requiring that, when the integration in Eq. (25) is from  $x'$  to 1, the parton densities at  $x''$  are half the parton densities at  $x''$ , when the integration takes place from  $x$  to 1.

The numerical solution of Eq. (25) was found using the CTEQ QCD evolution package. In order to illustrate the role, played by the shape of the input parton densities, two different

input parameterizations of Ref. [62] were considered: CTEQ4LQ with the starting scale of the evolution  $Q_0 = 0.7$  GeV and CTEQ4D with  $Q_0=1.6$  GeV. The parameterization CTEQ4LQ provides “valence-type” gluon and valence quark initial distributions localized around  $x = 0.2$ ; the input sea quark distribution is quite small. CTEQ4D gives slightly rising input parton distributions as  $x$  decreases.

The results for the path in the  $x - Q$ -plane for the gluon,  $u$  and  $s$  quark parton densities are presented in Fig. 10. CTEQ4LQ was used as an input. Each line represents a path, which begins at  $Q_0=1.6$  GeV and certain  $x'$  and ends at  $Q=5$  GeV and  $x = 10^{-4}$ , or  $10^{-3}$ , or  $10^{-2}$ . Each curve passes through  $1.6 \leq Q \leq 5$  GeV and  $x''$ , defined by the above algorithm. In Fig. 10, the upper panel corresponds to the implementation of our algorithm for the gluon parton density; the middle panel is for the  $u$  quarks; the lower one is for the  $s$  quark parton density.

From Fig. 10 one can see that the QCD evolution for gluons and quarks is different. The gluon density evolves in both  $Q$  and  $x$ ; the  $u$  quark evolves mostly in  $Q$  and turns sharply to reach the final point only at the end; the trajectory for the  $s$  quark is a mixture of the trajectories for the gluons and  $u$  quarks.

Note that the cross-over of the paths for the  $u$  quark in Fig. 10 is due to the following reason. At small  $x$ ,  $x = 10^{-4} \div 10^{-3}$ , the  $u$  quark parton density is rising and large. Hence, its support could come only from  $x \approx 0.2$ , where the input parton densities are peaked. This explains why the initial points of the corresponding paths are located at large  $x$ . On the other hand, the  $u$  quark parton density has a local minimum at  $x \approx 10^{-2}$  and, thus, the large support region in Eq. (25) is not required. This leads to the initial point at  $x \approx 0.06$  for the path, which ends at  $Q=5$  GeV and  $x = 10^{-2}$ .

Fig. 10 presents a *quantitative* approach to the path of the QCD evolution. One could arrive at the same *qualitative* conclusions simply by examining the corresponding parton densities at different  $Q$  as a function of  $x$ .

In the sense of the proposed algorithm, Fig. 10 answers the question: In Eq. (25), which regions of  $y$  at the input scale  $Q_0$  are important at higher  $Q > Q_0$ ? For example, one can see from Fig. 10 that at  $Q=5$  GeV and  $x = 10^{-4}$ , or  $x = 10^{-3}$ , or  $x = 10^{-2}$  half of the gluon parton density has come from  $x \geq 0.18 \div 0.22$  at  $Q_0=0.7$  GeV. This observation can be applied to an analysis of the QCD evolution of skewed parton densities in the proton and conventional parton densities in nuclei.

Let us assume that in the kinematics of a certain exclusive process, the skewedness parameter  $\Delta = x_{Bj}$  is small. Then, its effect is negligible at large values of  $x_1$ . We refer the reader to Subsect. II D for the definition of the kinematical variables. Since half of the contribution at small  $x_1$  and large  $Q$  has come from  $x_1 \geq 0.2$  at the input scale  $Q_0$ , the influence of the effects of  $\Delta$  will be decreased by at least 50% at small  $x_1$  and large  $Q$ . Therefore, this analysis justifies our claim that it is a good approximation to neglect the skewedness parameter  $\Delta$  in the input for the skewed QCD evolution.

Applying the result of Fig. 10 to the QCD evolution of conventional nuclear parton densities, one can readily explain the decrease of nuclear shadowing with the increase of  $Q$ . Since the major contribution at large  $Q$  and small  $x$  comes from larger  $x$  at the input scale  $Q_0$  where the effects of nuclear shadowing are not so significant, one would expect the effect of nuclear shadowing to decrease as  $Q$  increases.

Fig. 10 presents average paths. One can go one step further and study the influence of

various regions of  $y$  in Eq. (25) on the resulting parton densities in the final points and not only the average  $y$  that we called  $x'$  and  $x''$ . Such a study will help to answer the questions about the input for the skewed QCD evolution equation and the  $Q^2$  behaviour of nuclear shadowing in more detail.

To this end, let us introduce functions  $f_g(x, z)$  for gluons, defined as

$$f_g(x, z) = \frac{xG(x, Q=5)}{xG(x, Q=5)_z}, \quad (26)$$

and similar functions for quarks and antiquarks. Here  $xG(x, Q=5)$  is the gluon density at  $Q = 5$  GeV and  $x = 10^{-4}$ , or  $10^{-3}$ , or  $10^{-2}$ ;  $xG(x, Q=5)_z$  is the gluon density at the same  $Q$  and  $x$  but originated from Eq. (25), where the lower limit of integration is  $z$ . Thus, by definition  $f_g(x, x)=1$  and  $f_g(x, 1)=0$ .

$f(x, z)$  for gluon,  $u$  and  $s$  quark parton densities as a function of  $z$  are presented in Fig. 11. It helps to quantify further the importance of various regions of integration over  $y$  in Eq. (24). For example, from the upper panel of Fig. 11, one can see that at  $Q=5$  GeV and  $x=10^{-4}$ , 80% of the gluon density has come from  $y \geq 0.1$  at  $Q_0=0.7$  GeV.

We have also investigated how the QCD evolution path and the functions  $f_{g,u,s}(x, z)$  are affected by the choice of the input distribution for the QCD evolution equation. Figs. 12 and 13 represent the QCD evolution paths and functions  $f_{g,u,s}(x, z)$  for the case, when the parameterization CTEQ4D was used as the input. One can see that the fact that CTEQ4D input parton densities increase slightly as  $x$  decreases, affects the QCD evolution paths. While the general trend remains unchanged, the initial points for the paths shift to lower  $x$ .

In Fig. 13, one can see that at  $Q=5$  GeV and  $x=10^{-4}$ , 70% of the gluon density has come from  $y \geq 10^{-3}$  at  $Q_0=1.6$  GeV. Thus, if the skewedness parameter  $\Delta$  is of order  $10^{-4}$ , its effect is negligible at  $x_1 \approx 10^{-3}$ . Therefore, Fig. 13 quantitatively demonstrates that  $\Delta$  can be safely neglected in the input for the skewed QCD evolution.

The comparison of Figs. 10 and 12 demonstrates that the proposed algorithm for finding the path, along which the QCD evolution for the gluon and  $s$  quark parton densities proceeds, does not depend on the initial scale  $Q_0$ . Namely, the corresponding curves in Fig. 10 at  $Q=1.6$  GeV pass through almost exactly the same  $x'$  as in Fig. 12 at  $Q_0=1.6$  GeV. Thus, Figs. 10 and 12 can be used to analyze the QCD evolution of the gluons and  $s$  quarks between any two scales. A radically different input for the valence quarks for the two parameterizations, considered here, makes the corresponding evolution paths in the region  $1.6 \leq Q \leq 5$  GeV very different, and, thus, the universality discussed above does not hold.

In conclusion of this subsection, we would like to stress that our studies of the typical paths of the QCD evolution in the  $x-Q$ -plane presented in Figs. 10 and 12 demonstrate that the input for the skewed QCD evolution can be taken as the input for the QCD evolution of conventional parton densities as long the input densities are constant or grow insignificantly as  $x \rightarrow 0$  at the initial evolution scale  $Q_0$ . Such a behaviour at low  $x$  is constrained by the slow rise of cross sections for soft hadron-hadron interactions as energy increases.

## B. Numerical analysis of nuclear shadowing

In this subsection we will present our numerical studies of the  $Q^2$  and  $A$  dependence of skewed and ordinary parton densities in nuclei and nucleons using the QCD DGLAP

evolution equation. The studies serve the purpose of estimating numerically the regime of the onset of color transparency for hard exclusive and inclusive processes.

As explained in Sec. II, the kinematics of exclusive reactions dictates the use of skewed parton densities in evaluating cross sections of hard exclusive processes. In the limit of small and fixed  $x$  and large  $Q^2$ , the onset of color transparency manifests itself as the absence of nuclear shadowing in the ratio

$$R_G(x_1, \Delta, Q) = \frac{x g_A(x_1, x_2, Q^2)}{A x g_N(x_1, x_2, Q^2)} \rightarrow 1 . \quad (27)$$

As discussed in Subsect. III B, an additional  $A$  dependence in Eq. (27) due to the nuclear form factor is negligible at small  $x_{Bj}$ . Hence, the contribution due to the nuclear form factor was omitted in our numerical analysis<sup>5</sup>.

The numerical analysis of the conventional (non-skewed) QCD evolution equation was performed with the next-to-leading order in  $\alpha_s \log(Q^2/\Lambda^2)$  accuracy (NLO) using the CTEQ QCD evolution package. For the nucleon parton densities, we used the CTEQ4D parametrization with the starting evolution point  $Q_0=1.6$  GeV. The choice was motivated by the observation that the CTEQ4D gives a reasonable nonperturbative input: the gluon parton density is a rather flat function of Bjorken  $x$  at small  $x$  in accordance with physical intuition based on the slow rise with energy of soft hadron-hadron cross sections.

In order to carry out the numerical analysis of the skewed QCD evolution equation, we used a modified version of the CTEQ QCD evolution package [63]. In Subsect. IV A, it is explained why the input for the skewed QCD evolution can be taken as being equal to the input for the QCD evolution for conventional parton densities. Note that the detailed investigation of this issue showed that the input distribution should be fairly flat for this conjecture to be valid. Consequently, we started our QCD evolution with the input skewed parton densities  $g(x_1, x_2, Q_0^2) = x_1 G(x_1, Q_0^2)$  [43], where  $G(x_1, Q_0^2)$  is the conventional parton density. The accuracy of our calculations is of the leading order in  $\alpha_s \log(Q^2/\Lambda^2)$  (LO) because the skewed evolution kernels of the evolution package are implemented with the same accuracy. Hence, for the input nucleon parton densities we took the leading order in  $\alpha_s \log(Q^2/\Lambda^2)$  CTEQ4L parameterization with the starting evolution point  $Q_0=1.6$  GeV [62].

In order to account for significant nuclear shadowing at  $10^{-5} \div 10^{-4} \leq x \leq 0.05$  for gluon and sea quark nuclear parton densities and slight enhancement at  $0.05 \leq x \leq 0.2$  of the gluon nuclear parton density, we used the parameterization of Ref. [27]. This parameterization is based on the recent analysis of diffractive  $e p$  data of HERA, which revealed that the amount of shadowing in the gluon channel is approximately 3 times larger than was thought before.

Since gluons and valence quarks evolve separately at small  $x$ , one does not need to model shadowing and antishadowing for the valence quarks when studying the gluon parton density. Should one need to study nuclear modifications of valence quarks, one can assume that the valence quark parton densities are shadowed at small  $x$  and then enhanced at larger

<sup>5</sup>Note also that for semi-inclusive processes when a sum over nuclear fragmentation processes is taken, there is no suppression due to the nuclear form factor.

$x$ . However, one has to satisfy the baryon and momentum sum rules for the nuclear parton densities.

Results of the QCD evolution for nuclei with  $A = 12, 40, 100$  and  $200$  are presented in Figs. 6-8. Figs. 6 and 8 are the results of the QCD evolution of the conventional (diagonal) parton densities. The conventional QCD evolution is relevant for hard inclusive processes off nuclei such as DIS.

Fig. 6 illustrates decreasing nuclear shadowing due to the QCD evolution at high  $Q^2$  and fixed  $x$ . The ratio of the nuclear to nucleon gluon parton density per nucleon  $R_G(x, Q) = G_A(x, Q)/AG_N(x, Q)$  is plotted as a function of  $Q$  at  $x = 10^{-3}$ . One can see that the amount of shadowing for gluons, given by  $1 - R_G(x, Q)$ , decreases by a factor of 5 as  $Q$  increases from 1.6 to 15 GeV for nuclei with  $A = 12$  and  $A = 40$  and by approximately a factor of 4.5 for nuclei with  $A = 100$  and  $A = 200$ .

The onset of color transparency for exclusive processes (see also Eqs. (16) and (27)) is presented in Fig. 7. The ratio of nuclear to nucleon skewed gluon parton densities  $R_G(x_1, \Delta, Q) = g_A(x_1, x_2, Q)/Ag_N(x_1, x_2, Q)$  is plotted as a function of  $Q$  at fixed  $x_1 = 10^{-3}$  for different values of  $x_1 - x_2 = x_B; = \Delta$ . One can see that the curves for different  $\Delta$  for each  $A$  are remarkably close to each other. This is an interesting result because, even though the skewed gluon parton density is significantly larger than the diagonal one at small  $x$ , the effect of the skewedness  $\Delta$  (asymmetry) cancels almost exactly in  $R_G(x_1, \Delta, Q)$ . It can be explained by the fact that the QCD evolution does not change the difference  $x_1 - x_2$ , which is fixed by the kinematics of exclusive reactions. From Fig. 7 one can see that the amount of nuclear shadowing for gluons, given by  $1 - R_G(x_1, \Delta, Q)$ , decreases by approximately a factor of 3.5 as  $Q$  increases from 1.6 to 15 GeV for nuclei with  $A = 12, A = 40, A = 100$ , and  $A = 200$ .

Fig. 8 illustrates increasing nuclear shadowing in the limit  $x \rightarrow 0$ . At  $Q = 5$  GeV, when nuclear shadowing is still significant, the ratio  $1 - R_G(x, Q)$  increases by a factor of 10, when  $x$  is decreased from  $x = 10^{-2}$  to  $x = 10^{-4}$  for nuclei with  $A = 12$ , by approximately a factor of 8 for nuclei with  $A = 40$ , and by approximately a factor of 6 for nuclei with  $A = 100$  and  $A = 200$ .

Figs. 6, 8, and 7 demonstrate quantitatively that, as  $Q$  increases, nuclear shadowing decreases, and the regime of the generalized color transparency turns into the regime of color transparency.

### C. The unitarity boundary for the inelastic cross section and the phenomenon of perturbative color opacity

In this review we discuss coherent phenomena with nuclei at small Bjorken  $x$ . The main tool for the numerical analysis is the DGLAP QCD evolution equation. Then, the question arises: How low in  $x$  can one go before the evolution equation becomes unreliable?

One way to approach the answer to this question was presented in Ref. [7]. It is based on the observation that the inelastic small-size  $q\bar{q}$  dipole-nucleon cross section of Eq. (13), being of the leading twist, dominates over the elastic  $q\bar{q}$ -nucleon cross section, which is of the next-to-leading twist

$$\sigma^{inel} \gg \sigma^{el}. \quad (28)$$

When  $\sigma^{inel} \approx \sigma^{el}$ , the higher twist expression becomes of the same order as the leading twist term. Hence, the QCD evolution equation becomes inconsistent since it has generated large higher twist terms, which have been neglected in the derivation of the evolution equation.

This argument demonstrates that  $\sigma^{inel}$  given by Eq. (13) cannot grow infinitely at small  $x$  since that would destroy self-consistency of the DGLAP QCD evolution equation. The upper limit for  $\sigma^{inel}$  can be obtained from the constraint imposed by the unitarity of the  $S$ -matrix for purely QCD interactions and the optical theorem [7]

$$\sigma^{inel} \leq \frac{\pi r_N^2}{(1 + \beta^2)} = 22 \text{ mb} , \quad (29)$$

where  $r_N=0.8$  fm is the r.m.s. radius of the nucleon, which is measured in the electroproduction of vector mesons at large  $Q^2$  via the  $t$ -slope of the differential cross section;  $\beta \approx 0.4$  is the ratio of the real to imaginary parts of the elastic scattering amplitude.

In case of inclusive DIS on nuclear targets, the upper limit for the inelastic  $q\bar{q}$ -nucleus cross section  $\sigma_A^{inel}$  follows from the unitarity restriction

$$\sigma_A^{inel} \leq \frac{1}{2} \sigma_A^T = \pi R_A^2 , \quad (30)$$

where  $\sigma_A^T$  is the total  $q\bar{q}$ -nucleus cross section. Eq. (30) is applicable for sufficiently heavy nuclei when  $\sigma_A^T = 2\pi R_A^2$ , where  $R_A$  is the r.m.s. radius of the nucleus. Using  $R_A = 1.1A^{1/3}$  fm, one can write Eq. (30) in the form

$$\frac{\sigma_A^{inel}}{A} \leq \frac{38 \text{ mb}}{A^{1/3}} . \quad (31)$$

We studied Eqs. (29) and (31) numerically using the recently developed model for  $\sigma^{inel}$  [38]. The straightforward generalization of Eq. (13) for the color triplet ( $q\bar{q}$  fluctuation) and color octet ( $q\bar{q}g$  fluctuation) dipole scattering cross sections on the nuclear target reads

$$\begin{aligned} \sigma_A^{q\bar{q}}(b^2, x') &= \frac{\pi^2}{3} b^2 \left[ x' G_A(x', \lambda/b^2) \right] \alpha_s(\lambda/b^2) , \\ \sigma_A^{q\bar{q}g}(b^2, x') &= \frac{3\pi^2}{4} b^2 \left[ x' G_A(x', \lambda/b^2) \right] \alpha_s(\lambda/b^2) . \end{aligned} \quad (32)$$

In our numerical analysis, the nuclear gluon parton density  $x' G_A(x', \lambda/b^2)$  was parameterized as the product of the factor describing shadowing at  $10^{-5} \leq x' \leq 0.05$  and antishadowing at  $0.05 \div 0.1 \leq x' \leq 0.2$  according to Ref. [27], and the gluon parton density of the proton. We used the leading order parton parameterization CTEQ4L in Eqs. (29) and (31) since the expressions for the inelastic  $q\bar{q}$ -nucleon ( $q\bar{q}g$ -nucleon) and  $q\bar{q}$ -nucleus ( $q\bar{q}g$ -nucleus) cross sections have been derived in the leading  $\alpha_s(Q^2) \log(Q^2/\Lambda^2)$  approximation.

The solutions of Eqs. (29) and (31) are presented in Figs. 14-17. For each given  $Q_{eff} = \sqrt{\lambda}/b$ , the liming value of  $x'$ , which is denoted  $x_{lim}$ , at which Eqs. (29) and (31) are still satisfied, was found. Thus, the kinematics regions allowed by the unitarity restrictions lie to the right of the corresponding curves.

In Fig. 14, we plot  $x_{lim}$  as a function of  $Q^2$  for nuclei with  $A=12, 40, 100$  and  $200$ , and for the nucleon. One can see that, for nuclei with  $A=200, 100$  and  $40$ , the kinematics

constraints are more stringent than for the nucleon. Thus, the breakdown of the DGLAP QCD evolution equation occurs sooner, i.e. at larger  $x$  for a given  $Q$ , for heavy nuclei than for the proton.

Note that, for heavy enough nuclei, one can select scattering at central impact parameters by taking pairs of nuclei like  $^{208}\text{Pb}$  and  $^{40}\text{Ca}$ . Since the nuclear thickness at small impact parameters is about a factor of 1.5 larger than the average nuclear thickness, and since the average nuclear thickness is  $\propto A^{1/3}$  the plots for  $A=40, 100$  and  $200$  roughly correspond to scattering at the central impact parameters on nuclei with  $A' \approx A/(1.5)^3$ .

In Fig. 15, we plot  $x_{lim}$  as a function of  $Q^2$  for nuclei with  $A=200$ . We present three scenarios of gluon shadowing in nuclei. The solid curve corresponds to nuclear shadowing parameterized as in [27] (it is the same curve as in Fig. 14). The dashed curve corresponds to a smaller amount of shadowing. In this case, gluons are shadowed as the sea quarks in [27]. The dotted curve is for the situation, when nuclear effects are neglected. In all three cases, at each given  $Q$ ,  $x_{lim}$  is larger than the corresponding  $x_{lim}$  for the proton target.

Figs. 16 and 17 represent the unitarity boundary for the inelastic  $q\bar{q}g$  (color octet) fluctuation scattering cross section on nuclear and nucleon targets, which is given by combining Eqs. (31) and (32). While the trend is quite similar to Figs. 14 and 15, the unitarity boundary is much more stringent –  $x_{lim}$  is greater by more than the order of magnitude at the corresponding  $Q_{eff}$ .

The phenomenon of  $\sigma^{inel}$  being large at small transverse size  $b$  and small  $x$  is called color opacity phenomenon. The regime of color opacity corresponds to a small coupling constant  $\alpha_s(Q^2)$  and large parton densities. Figs. 14 and 15 demonstrate that it is more advantageous to study the physics of color opacity with heavy nuclei than with the proton. The latter observation can be explained by the fact that the density of partons per nucleon, even when one takes into account significant nuclear shadowing, is larger for heavy nuclei than for the proton.

The regime of color opacity is a new field of QCD. It becomes accessible at larger  $x$  for heavy nuclei than for the proton target. Hence, it should be feasible to study color opacity at LHC [7,64], HERA with nuclear beams [7,65], and eRHIC.

## V. SOFT DIFFRACTIVE DISSOCIATION ON NUCLEI

The present section is concerned with applications of the principles of color coherence to the domain of soft physics – diffractive dissociation of hadrons on nuclei and nuclear shadowing in hadron-nuclear collisions. Color or cross section fluctuations constitute the basis of a phenomenological description of all the available data on diffractive dissociation and nuclear shadowing on light and heavy nuclei.

### A. Diffractive dissociation as a manifestation of the coherence length and color fluctuations

As discussed in the Introduction, one of the principles of color coherence phenomena in QCD is that an energetic hadronic projectile consists of coherent quark-gluon configurations of very different spatial sizes. These quark-gluon configurations are called color

fluctuations. They can also be called cross section fluctuations since the configurations with different transverse sizes interact with the target with different cross sections. Cross section fluctuations become significant, when the coherence length  $l_c$  is large. The importance of the large  $l_c$  in diffractive dissociation of hadrons was first discovered in [66].

It is important to note that one has to distinguish two phenomenological descriptions of strong interactions. In the description, which is more relevant for hard processes, the color fluctuations are quark-gluon configurations of small sizes, which are almost fixed. The masses of such fluctuations are undefined. The other description, which is natural for diffractive dissociation, operates with physical particles of fixed masses. Then, it is more appropriate to consider the distribution over transverse sizes. Using the principles of color coherence, one can naturally relate the two descriptions of strong interactions.

Let us consider diffractive dissociation of a hadron with mass  $m$  and large momentum  $p_{lab}$  on a hadronic target  $T$  in the laboratory reference frame. The incoming hadron can fluctuate into a hadronic state with mass  $M^*$  due to the uncertainty principle. The coherence length  $l_c$  corresponds to the time, during which the incoming hadron stays in the state with mass  $M^*$ ,

$$l_c = \frac{1}{\Delta E} = \left( \sqrt{M^{*2} + p_{lab}^2} - \sqrt{m^2 + p_{lab}^2} \right)^{-1} \simeq \frac{2p_{lab}}{M^{*2} - m^2}. \quad (33)$$

From Eq. (33), one can immediately see that the coherence length grows with the energy of the incoming hadron (which is proportional to  $p_{lab}$ ).

If the coherence length is greater than the typical size of the target  $2R_T$ ,

$$l_c \geq 2R_T, \quad (34)$$

then all the fluctuations, whose masses satisfy Eqs. (33) and (34), interact coherently with the entire target. This fact has three consequences. Firstly, as energy grows, more diffractive states of ever-increasing mass can be produced. Secondly, the large  $l_c$  corresponds to small momentum transfers to the target. It means that the target (nucleon or nucleus) has a large probability to remain in its ground state while the interaction takes place. Moreover, if the target is a nucleus, the suppression of the scattering amplitude due to the nuclear form factor is small. The first and second consequences manifest themselves in a large probability of coherent diffractive processes on nuclei. Thirdly, the coherence of the fluctuations means that they can be considered as frozen during the interaction with the target. This enables one to introduce a function  $P(\sigma)$ , which gives the probability to find a hadronic (quark-gluon) configuration, which interacts with the target with the cross section  $\sigma$ , in the energetic projectile.  $P(\sigma)$  can be most naturally introduced within the framework of the basis of states, which consists of configurations of definite scattering cross sections with the target [67].

The vector of state of an energetic incident hadron  $|\Psi\rangle$  can be represented as a coherent superposition of eigenstates  $|\Psi_k\rangle$  of the scattering matrix

$$|\Psi\rangle = \sum_k c_k |\Psi_k\rangle, \quad (35)$$

where

$$\begin{aligned} \text{Im}T|\Psi_k\rangle &= t_k|\Psi_k\rangle , \\ \sum_k |c_k|^2 &= 1 . \end{aligned} \quad (36)$$

Here,  $T$  is the scattering operator, and  $t_k$  is the imaginary part of the eigenvalue corresponding to the eigenstate  $|\Psi_k\rangle$ .

Since various states  $|\Psi_k\rangle$  interact with the target with different cross sections  $\sigma_k$ , which, by the optical theorem, are related to the imaginary part of the scattering amplitude  $t_k$ ,

$$\sigma_k = t_k , \quad (37)$$

the coherent superposition of the eigenstates, which forms the final state emerging after the scattering, could be different from the initial state. Thus, the formalism of eigenstates of the scattering matrix is natural for describing diffractive dissociation of hadrons.

Using Eqs. (35)-(37), diffractive dissociation can be presented as follows. Diffractive scattering occurs when the final state carries the same quantum numbers as the initial state, i.e. whenever the initial state overlaps any  $|\Psi_k\rangle$ . Then, the total diffractive differential cross section at  $t = 0$  can be presented as

$$\left(\frac{d\sigma}{dt}\right)_{t=0}^{\text{diff}} = \frac{1}{16\pi} \sum_k |\langle\Psi_k| \text{Im}T |\Psi\rangle|^2 = \frac{1}{16\pi} \sum_k |c_k|^2 t_k^2 \equiv \frac{1}{16\pi} \langle\sigma^2\rangle . \quad (38)$$

In Eq. (38), we have used the completeness of the set of states  $|\Psi_k\rangle$  and the optical theorem (37). We have also introduced the second moment  $\langle\sigma^2\rangle$  of the distribution over cross sections  $P(\sigma)$ . Similarly, the elastic diffractive differential cross section at  $t = 0$  reads

$$\left(\frac{d\sigma}{dt}\right)_{t=0}^{\text{el}} = \frac{1}{16\pi} |\langle\Psi| \text{Im}T |\Psi\rangle|^2 = \frac{1}{16\pi} \left( \sum_k |c_k|^2 t_k \right)^2 \equiv \frac{1}{16\pi} \langle\sigma\rangle^2 , \quad (39)$$

where  $\langle\sigma\rangle$  is the first moment of  $P(\sigma)$ .

Subtracting the elastic cross section from the total diffractive cross section, one obtains the diffractive dissociation cross section (inelastic diffractive cross section)

$$\left(\frac{d\sigma}{dt}\right)_{t=0}^{\text{inel}} = \left(\frac{d\sigma}{dt}\right)_{t=0}^{\text{diff}} - \left(\frac{d\sigma}{dt}\right)_{t=0}^{\text{el}} = \frac{1}{16\pi} (\langle\sigma^2\rangle - \langle\sigma\rangle^2) . \quad (40)$$

Eq. (40) was first derived in [68] in order to describe diffractive dissociation within the framework of cross section fluctuations. Eq. (40) explicitly demonstrates that diffractive dissociation occurs only if different components  $|\Psi_k\rangle$  of the incident hadron interact with the target with different strengths  $t_k$ , i.e. when cross section fluctuations take place in the wave function of the incoming hadron.

## B. Properties of $P(\sigma)$

The formalism of scattering matrix eigenstates provides an economic way to take into account the composite structure of energetic projectiles. Due to the frozenness condition, each state  $|\Psi_k\rangle$  scatters independently on the target and then contributes coherently to

the final state with the probability  $|c_k|^2$ , see also Eq. (35). Then, one can introduce the distribution over cross sections  $P(\sigma)$  [1]

$$P(\sigma) = \sum_k |c_k|^2 \delta(\sigma - \sigma_k) . \quad (41)$$

One can see from Eq. (41) that it is the composite nature of hadrons that gives rise to the term cross section fluctuations.

The cross section distribution function  $P(\sigma)$  comprises perturbative and non-perturbative information on the wave function of the hadron. The modelling of  $P(\sigma)$  involves pQCD calculations, valid at small  $\sigma$ , and constraints on first moments of  $\sigma$ , extracted from experiments. In addition, it is required that  $P(\sigma) \rightarrow 0$  at  $\sigma \rightarrow \infty$ .

The quark counting rule fixes the low- $\sigma$  behaviour of  $P_h(\sigma)$  for hadrons [69]

$$P_h(\sigma) \propto \sigma^{n_q-2} , \quad (42)$$

where  $n_q$  is the number of valence quarks in the hadron. Thus, for protons, when  $\sigma$  is much smaller than the average value of  $\sigma$ , i.e. when  $\sigma \ll \langle \sigma \rangle$ , one obtains that

$$P_p(\sigma) \sim \sigma . \quad (43)$$

For pions, the quark counting rule predicts at  $\sigma \ll \langle \sigma \rangle$  [69]

$$P_\pi(\sigma) \sim \text{const} . \quad (44)$$

However, one can go further than the simple counting rule in case of pions. In order to find  $P_\pi(\sigma)$  at  $\sigma \ll \langle \sigma \rangle$ , one can apply the QCD factorization theorem [1,69] and find the constant entering Eq. (44):

$$P_\pi(\sigma) = \frac{6f_\pi^2}{5\alpha_s(4k_t^2)\bar{x}G_N(\bar{x}, 4k_t^2)} . \quad (45)$$

In this equation,  $\alpha_s(4k_t^2)$  is the QCD running coupling constant;  $G_N(\bar{x}, 4k_t^2)$  is the gluon distribution in the nucleon;  $\bar{x} = 4k_t^2/s_{\pi N}$ , where  $s_{\pi N}$  is the center of mass energy squared;  $k_t^2 \propto 1/b^2$ , where  $b$  is the transverse size of the  $q\bar{q}$  pair of the wave function of the pion;  $f_\pi$  is the constant for the  $\pi \rightarrow \mu\nu$  decay.

Note that the calculations of the cross section of exclusive electroproduction of vector mesons [21] and that of  $P_\pi(\sigma)$  [1,69] use a similar technique. Therefore, the confirmation of the results of [21] by the ZEUS data at HERA [14] provides an indirect confirmation of the calculation of  $P_\pi(\sigma \ll \langle \sigma \rangle)$ .

Using the QCD factorization theorem, one can compute  $P_\gamma(\sigma)$  for photons at  $\sigma \ll \langle \sigma \rangle$ . It was found that the behaviour of  $P_\gamma(\sigma)$  at small  $\sigma$  is divergent [37]

$$P_\gamma(\sigma) \propto \frac{1}{\sigma} . \quad (46)$$

Such a behaviour is consistent with the quark counting rule of Eq. (38). Since the quark and antiquark in the photon wave function are created at the same point, they have a large probability to stay close to each other.

Suggested parameterizations of the proton and pion distribution functions  $P(\sigma)$  describe correctly the above discussed behaviour at small and large  $\sigma$  [69]

$$\begin{aligned} P_p(\sigma) &= N(a, n) \frac{\sigma/\sigma_0}{\sigma/\sigma_0 + a} e^{-(\sigma-\sigma_0)^n/(\Omega\sigma_0)^n}, \\ P_\pi(\sigma) &= N(a, n) e^{-(\sigma-\sigma_0)^n/(\Omega\sigma_0)^n}. \end{aligned} \quad (47)$$

$P_p(\sigma)$  and  $P_\pi(\sigma)$  as functions of  $\sigma$  are presented in Fig. 18 [69].

The free parameters of the parameterizations (47) are chosen in order to satisfy the following constraints on the first few moments of the distribution  $P(\sigma)$ :

$$\begin{aligned} \int P(\sigma) d\sigma &= 1, \\ \int P(\sigma) \sigma d\sigma &= \langle \sigma \rangle, \\ \int P(\sigma) \sigma^2 d\sigma &= \langle \sigma^2 \rangle = (1 + \omega_\sigma) \langle \sigma \rangle^2, \\ \int P(\sigma) (\sigma - \langle \sigma \rangle)^3 d\sigma &\approx 0. \end{aligned} \quad (48)$$

The first equation is the normalization of  $P(\sigma)$ . The first moment  $\langle \sigma \rangle$  is the total hadron-nucleon cross section.

The third of Eqs. (48) is a relation between the second moment  $\langle \sigma^2 \rangle$  and the quantity  $\omega_\sigma$ . Using Eq. (40), one can write that

$$\omega_\sigma = \frac{\left(\frac{d\sigma}{dt}\right)_{t=0}^{inel}}{\left(\frac{d\sigma}{dt}\right)_{t=0}^{el}} = \frac{\langle \sigma^2 \rangle - \langle \sigma \rangle^2}{\langle \sigma \rangle^2}, \quad (49)$$

which demonstrates that  $\omega_\sigma$  is proportional to the amount of diffractive dissociation.  $\omega_\sigma$  can be extracted from the experiment. From the data on the total cross section of neutron-deuteron scattering [70] and from the theoretical analysis of [71], which used the proton-deuteron data [72],  $\omega_\sigma=0.25$  for  $p_{lab} \approx 200$  GeV/c. Another source of information on  $\omega_\sigma$  is the data on diffractive dissociation on hydrogen. The data leads to a similar value of  $\omega_\sigma$  [69].

The last equation in Eq. (48) is based on the analysis of [69] of the data on coherent diffractive dissociation of protons on deuteron [73]. It indicates that  $P_p(\sigma)$  is symmetrical around its average value. In order to impose further restriction of higher moments of  $P(\sigma)$ , one has to consider diffractive dissociation on heavier nuclei, for example, on  ${}^4\text{He}$ .

### C. Total and diffractive dissociation cross sections of hadron-deuteron scattering

In the previous subsection we demonstrated that in order to study the second moment of  $P(\sigma)$ ,  $\langle \sigma^2 \rangle$ , one can study either diffractive dissociation on hydrogen (see Eq. (40)) or the total hadron-deuteron cross section. In this subsection, the latter approach is considered in detail.

As discussed in Subsec. II A, there is a deep connection between high energy diffraction of hadrons on the proton and nuclear shadowing in the total hadron-nucleus cross section. Using the space-time picture of high energy scattering, which follows from the quantum field

theory, V. Gribov has derived the total cross section of hadron-deuteron scattering  $\sigma_{tot}^{hD}$  [25] (see also Eq. (5))

$$\sigma_{tot}^{hD} = \sigma_{tot}^{hp} + \sigma_{tot}^{hn} - \frac{1}{4\pi} \int dt S(4t) \left( \int dM^2 \frac{d^2\sigma^{h+p \rightarrow X+p}}{dM^2 dt} + \frac{d\sigma^{h+p \rightarrow h+p}}{dt} \right), \quad (50)$$

where  $\sigma_{tot}^{hp}$  and  $\sigma_{tot}^{hn}$  are the total hadron-proton and hadron-neutron cross sections;  $d^2\sigma/dM^2 dt$  is the cross section for producing a diffractive state  $X$  with mass  $M$  in the reaction  $h + N \rightarrow X + N$ ;  $t$  is the squared four-momentum transfer;  $S(t)$  is the electromagnetic form factor of the deuteron. For simplicity, spin effects in the wave function of the deuteron and the real part of the diffractive scattering amplitude have been neglected.

In spite of different space-time evolution pictures of scattering processes in quantum field theory and in non-relativistic quantum mechanics, Eq. (50) generalizes the earlier result of [74], when only the second term in the bracket of Eq. (50) (elastic shadowing) was taken into account.

Eq. (50) relates the amount of nuclear shadowing in the total cross section of hadron-deuteron scattering to the cross section of diffractive dissociation of the hadron on the proton. Nuclear shadowing due to diffractive dissociation (inelastic diffraction) is called inelastic shadowing because it is caused by the excitation and propagation of inelastic intermediate states. Fig. 1 depicts that the inelastic shadowing term appears due to the interference between the diffractive scattering of the incident hadron off the proton and the neutron of the deuterium target. Although inelastic shadowing corrections are rather small for hadron-nucleus collisions, inelastic shadowing is the only mechanism, which relates nuclear shadowing in inclusive DIS on nuclei to diffraction in DIS on proton.

Within the formalism of cross section fluctuations, Eq. (50) was rederived in [75],

$$\sigma_{tot}^{hD} = 2\langle\sigma\rangle - \frac{\langle\sigma^2\rangle}{8\pi^2} \int e^{-q^2\beta} S(q) d^2q. \quad (51)$$

Here, it is assumed that  $\sigma_{tot}^p = \sigma_{tot}^n = \langle\sigma\rangle$  and that the spin effects in the deuteron wave function and the real part of the diffractive scattering amplitude are negligible. Eq. (51) explicitly demonstrates how  $\langle\sigma^2\rangle$  and  $\omega_\sigma$  can be extracted from the shadowing term in the total hadron-deuteron cross section. Using the data on elastic and inelastic shadowing in  $\sigma_{tot}^{nD}$  [70] and  $\sigma_{tot}^{pD}$  [72] (see also [71]), one finds that  $\omega_\sigma(p, n) = 0.25$  for the average values of  $p_{lab}$ ,  $p_{lab}=200$  GeV/c.

For a pion projectile, the value of  $\omega_\sigma(\pi)=0.4$  at  $p_{lab}=200$  GeV/c was extracted in [76] from the data on  $\pi D$  scattering of [72]. This value of  $\omega_\sigma$  is in accord with the theoretical expectations, ensuing from the quark counting rule and the triple Pomeron exchange model. The larger value of  $\omega_\sigma(\pi)$  for pions than for protons means that the distribution over cross sections  $P(\sigma)$  is broader for pions than that for protons. This fact is reflected in the parameterizations (47).

A direct comparison of Eqs. (49), (50) and (51) enables one to identify  $\omega_\sigma$  as the ratio of the diffractive dissociation to elastic cross sections

$$\omega_\sigma = \frac{\langle\sigma^2\rangle - \langle\sigma\rangle^2}{\langle\sigma\rangle^2} = \left( \int \int S(4t) \frac{d^2\sigma^{h+p \rightarrow X+p}}{dM^2 dt} dM^2 dt \right) / \left( \int S(4t) \frac{d\sigma^{h+p \rightarrow h+p}}{dt} dt \right). \quad (52)$$

Eq. (52) explicitly demonstrates the connection between diffractive dissociation, inelastic nuclear shadowing, and cross section fluctuations.

The third moment  $\langle\sigma^3\rangle$  of  $P_h(\sigma)$  can be found by considering diffractive dissociation of the hadron  $h$  on deuteron. The reaction  $p + D \rightarrow X + D$  was analyzed in [69], where the ratio of the proton coherent diffractive dissociation cross sections on deuterons and hydrogen was presented as

$$\left(\frac{d\sigma_{diff}}{dt}\right)_{t=0}^{pD}/\left(\frac{d\sigma_{diff}}{dt}\right)_{t=0}^{pp} = 4 - \frac{1}{2\pi^2} \frac{\langle\sigma^3\rangle - \langle\sigma\rangle\langle\sigma^2\rangle}{\langle\sigma^2\rangle - \langle\sigma\rangle^2} \int d^2 p_\perp S(p_\perp). \quad (53)$$

Using Eq. (53) and the data on coherent diffraction of protons on deuterium [73], one arrives at  $\int P_p(\sigma)(\sigma - \langle\sigma\rangle)^3 d\sigma \approx 0$  (see [69] for details).

#### D. Diffractive dissociation on $\text{He}^4$

In order to study further the importance of color fluctuations in energetic hadrons and higher moments of the distribution  $P(\sigma)$ , one should consider heavier nuclei. The only existing experimental data on inclusive coherent diffraction on light nuclei is the data on proton diffractive dissociation on  $\text{He}^4$  in the reaction  $p + \text{He}^4 \rightarrow X + \text{He}^4$  [77].

Using the cross section (color) fluctuation formalism along with the Gribov-Glauber multiple scattering formalism [25,74], the ratio of diffractive differential cross section on  $\text{He}^4$  and on the proton at  $t = 0$  can be presented as a series over moments of  $P_p(\sigma)$  [78]

$$\begin{aligned} \left(\frac{d\sigma_{diff}}{dt}\right)_{t=0}^{p\text{He}} / \left(\frac{d\sigma_{diff}}{dt}\right)_{t=0}^{pp} &= 16 - \frac{6\gamma}{\omega_\sigma} \left( \frac{\langle\sigma^3\rangle}{\langle\sigma\rangle^3} - \frac{\langle\sigma^2\rangle}{\langle\sigma\rangle^2} \right) + \frac{59\gamma^2}{48\omega_\sigma} \left( \frac{\langle\sigma^4\rangle}{\langle\sigma\rangle^4} - \frac{27\langle\sigma^2\rangle^2}{59\langle\sigma\rangle^4} - \frac{32\langle\sigma^3\rangle}{59\langle\sigma\rangle^3} \right) \\ &\quad - \frac{5\gamma^3}{32\omega_\sigma} \left( \frac{\langle\sigma^5\rangle}{\langle\sigma\rangle^5} - \frac{4\langle\sigma^3\rangle\langle\sigma^2\rangle}{5\langle\sigma\rangle^5} - \frac{1\langle\sigma^4\rangle}{5\langle\sigma\rangle^4} \right). \end{aligned} \quad (54)$$

Here,  $\langle\sigma\rangle = 41$  mb is the total hadron-nucleon cross section at  $p_{lab} = 200$  GeV/c. The parameter  $\gamma$ , defined as  $\gamma = \langle\sigma\rangle/\pi(\alpha + \beta)$ , emerges from the integration over transverse momenta of the proton-nucleon scattering amplitudes with the  $\text{He}^4$  ground state wave function;  $\alpha = 23$  (GeV/c) $^{-2}$  is the slope of the ground state wave function of  $\text{He}^4$ , which is parameterized in the exponential form [29];  $\beta = 10.5$  (GeV/c) $^{-2}$  is the slope of hadron-nucleon cross section, which is taken as the average of the slopes of the elastic and diffractive cross sections [78]. This yields  $\gamma = 1.01$ .

Then, using the parameterization (47) in order to compute the higher moments of  $P_p(\sigma)$ , Eq. (54) leads to [78]

$$r = \left(\frac{d\sigma_{diff}}{dt}\right)_{t=0}^{p\text{He}} / \left(\frac{d\sigma_{diff}}{dt}\right)_{t=0}^{pp} = 6.8 \div 7.6. \quad (55)$$

The lower value of  $r$  corresponds to  $n = 2$  in Eq. (47), and the upper value of  $r$  corresponds to  $n = 6$  and  $n = 10$  in Eq. (47).

Eq. (55) is in an excellent agreement with the experimental data on proton coherent diffractive dissociation on helium [77]. Integrating the data over the available range of diffractive masses  $2.5 \leq M^2 \leq 8$  GeV $^2$ , it was found in [78] that

$$r^{exp} = 7.1 \pm 0.7. \quad (56)$$

Here, the main error originates from the extrapolation of the data to  $t = 0$ . It is important to note that, although the comparison to the theoretical value of  $r$  implies the integration over all diffractive masses  $M^2$ , the correction, related to the inclusion of non-measured small diffractive masses, is small [78].

The remarkable agreement between the theory and experiment demonstrates that, indeed, significant color fluctuations (cross section fluctuations) are present in energetic protons. The phenomenological description of those fluctuations by Eq. (47), which is based on the notion of color fluctuations, successfully reproduces the existing experimental data on diffraction on helium and heavier nuclei (see Subsect. V E) with an accuracy of 10% without introducing any new free parameters. The latter fact is a sign of universality of the description that uses the distribution over cross sections  $P(\sigma)$ .

One can also compare the theoretical prediction with the data on the total diffractive cross section of proton- ${}^4\text{He}$  scattering. Combining the Gribov-Glauber multiple scattering formalism, cross section fluctuations and the parameterizations (47), the total coherent diffractive cross section of proton- ${}^4\text{He}$  scattering  $\sigma_{He-4}^{diff}$  was obtained in [79]

$$\begin{aligned}\sigma_{He-4}^{diff} &= 3.5 \text{ mb}, \quad n = 2, \\ \sigma_{He-4}^{diff} &= 3.7 \text{ mb}, \quad n = 6, 10.\end{aligned}\tag{57}$$

The result of Eq. (57) is in a good agreement with the experimental data of [77], integrated over  $0.04 \text{ GeV}^2 \leq |t| \leq 0.4 \text{ GeV}^2$  and over diffractive masses  $0 \text{ GeV}^2 \leq M^2 \leq 10 \text{ GeV}^2$ :

$$\sigma_{He-4}^{diff}(exp) = 2.6 \pm 0.9 \text{ mb}.\tag{58}$$

In Eq. (58), the error is dominated by the uncertainty of the extrapolation of the experimental data into the unmeasured regions of small  $t \leq 0.04 \text{ GeV}^2$  and small diffractive masses  $M^2 \leq 1.2 \text{ GeV}^2$ .

Fig. 19 presents a comparison of the theoretical predictions for the total cross sections of coherent diffraction of protons and neutrons on nuclei to the available experimental data. The value of  $\sigma_{He-4}^{diff}(exp)$ , given by Eq. (58), is presented as a full circle. The theoretical prediction for  $\sigma_{He-4}^{diff}$ , given by Eq. (57), is presented by two dashed curves that correspond to  $n = 2$  (lower curve) and  $n = 6$  and  $n = 10$  (upper curve).

## E. Diffractive dissociation on heavy nuclei

Cross section (color) fluctuation formalism can also be successfully applied to diffractive dissociation on heavy nuclei. For heavy nuclei, one can neglect the slope of the elementary hadron-nucleon elastic scattering amplitude as compared to the slope of the nuclear wave function as well as correlations in the nuclear wave function. Then, in this approximation, the coherent diffractive dissociation cross section  $\sigma_{diff}^{hA}$  of hadrons  $|h\rangle$  on the nucleus with the atomic number  $A$  can be presented as [80]

$$\sigma_{diff}^{hA} = \int d^2 b \left( \int d\sigma P_h(\sigma) \sum_n |\langle h | F(\sigma, b) | n \rangle|^2 - \left( \int d\sigma P_h(\sigma) |\langle h | F(\sigma, b) | h \rangle| \right)^2 \right),\tag{59}$$

where  $b$  is the impact parameter;  $|n\rangle$  is the diffractively produced final state;  $F(\sigma, b)$  is the Glauber profile function, defined as  $F(\sigma, b) = 1 - e^{-\sigma T(b)/2}$ , where  $T(b) = \int_{-\infty}^{\infty} \rho_A(b, z) dz$ ,  $\rho_A(b, z)$  is the nuclear density. Using completeness of the states  $|n\rangle$ ,  $\sigma_{diff}^{hA}$  can be presented as

$$\sigma_{diff}^{hA} = \int d^2b \left( \int d\sigma P_h(\sigma) |\langle h | F^2(\sigma, b) | h \rangle| - \left( \int d\sigma P(\sigma) |\langle h | F(\sigma, b) | h \rangle| \right)^2 \right). \quad (60)$$

The theoretical prediction of Eq. (60) for protons (neutrons) is compared to the experimental data in Fig. 19, where  $\sigma_{diff}^{pA}$  is presented as a function of  $A$ . The three solid curves correspond to the calculation with  $n=2, 6$  and  $10$  of the parameterization (47). The  $A$  dependence of  $\sigma_{diff}^{pA}$  is of the approximate form  $A^{0.8}$  for  $A \approx 16$  and  $A^{0.4}$  for  $A \approx 200$ . There are only two sets of experimental data on coherent nuclear diffraction of nucleons on heavy nuclei – the data on  $n + A \rightarrow p\pi^- + A$  for the mass interval  $1.35 \leq M \leq 1.45$  GeV [81] and the data for emulsion targets [82]. In Fig. 19, the data of [81] is presented as stars and the data of [82] is presented as triangles.

As one can see from Fig. 19, the theoretical prediction of the  $A$  dependence of coherent diffraction of protons and neutrons on nuclei, based on color fluctuations accumulated in  $P_p(\sigma)$ , reproduces the experimental data well. Note that the data points for the reaction  $n + A \rightarrow p\pi^- + A$  lie systematically below the theoretical (solid) curves because the data points represent only one channel (a particular final state) of the total diffractive cross section.

For pion projectiles, the approach, which uses  $P_\pi(\sigma)$ , also describes the available experimental data well [80].

Inelastic diffraction (diffractive dissociation) on nuclei arises due to scattering at impact parameters that are rather close to the nuclear surface, where the nucleus is not so opaque and the nuclear density is small. The dominant contribution to inelastic diffraction comes from the fluctuations of the projectile, whose size is close to the average size of the projectile. This fact can be seen from the approximate diffractive cross section  $\sigma_{diff}^{appr\,hA}$ , which was computed by expanding  $F(\sigma, b)$  about  $\sigma = \langle \sigma \rangle$  in Eq. (59) [80]

$$\sigma_{diff}^{appr\,hA} = \frac{\omega_\sigma \langle \sigma \rangle^2}{4} \int d^2b T(b)^2 e^{-\langle \sigma \rangle T(b)}. \quad (61)$$

Eq. (61) is quantitatively accurate for  $A \leq 50$  and qualitatively good for all  $A$ . It demonstrates that the  $A$  dependence is mainly determined by the value of  $\langle \sigma \rangle$ . For  $A \geq 50$ , Eq. (61) gives a weaker  $A$  dependence than the exact formula (59). The deviation at large  $A$  should come from configurations with relatively small  $\sigma$ .

It is important to note that the numerical analysis of [80] shows that it is impossible to study the dominance of small size contributions in reactions of coherent nuclear diffraction simply by increasing  $A$ , because it requires unreasonably heavy nuclei. Consequently, one should explore the domain of hard diffraction in the search for the dominance of small-size configurations.

## F. Cross section fluctuations in heavy-ion collisions

Color fluctuations also play an important role in inelastic reactions with nuclei. The effect of color fluctuations in the wave function of hadrons on multiplicity of binary nucleon-nucleon

collisions and the transverse energy production in central high-energy nuclear collisions was calculated in [83]. It was found that the color fluctuations account for the large multiplicity of binary nucleon-nucleon collisions and the transverse energy fluctuations found experimentally. The fluctuation parameter  $\omega_\sigma$  (see Eq. (49)) increases at  $\sqrt{s} \leq 60$  GeV and decreases for  $\sqrt{s} \geq 400$  GeV. Thus,  $\omega_\sigma$  is likely to be close to its maximum,  $\omega_\sigma \sim 0.3 \div 0.35$ , for the energies to be studied in  $AA$  collisions at RHIC. Therefore, the effects of color fluctuations in the hadron wave function are relevant for the RHIC program and should be included in the event generators of central nucleus-nucleus collisions.

## VI. CONCLUDING REMARKS

We find that QCD unambiguously predicts the onset of color transparency in hard coherent meson electroproduction on nuclei at small Bjorken  $x$  and  $Q \rightarrow \infty$ . Thus, coherent hard phenomena are now becoming an effective instrument in the investigation of the quark-gluon structure of hadrons and nuclei.

At the moment, there are many uncertainties in the subject of extremely small Bjorken  $x$  phenomena, where the QCD evolution equation becomes inapplicable. However, the conclusion that the onset of the new QCD regime of large parton densities can be achieved in  $eA$  collisions at HERA and  $p\bar{p}$  collisions at LHC, seems to be model-independent.

## VII. ACKNOWLEDGEMENTS

We thank our collaborators S. Brodsky, J. Collins, A. Freund, W. Koepf, G.A. Miller, A.H. Mueller, M. McDermott, and A. Radyushkin who have contributed to many of the analyses discussed in the review. We are indebted to N. Auerbach for fruitful discussions of isobaric excitations in electroweak transitions, and to L. Gerland for valuable comments. V.G. would like to thank J. Collins for providing the CTEQ QCD evolution package.

This work was supported by the U.S. Department of Energy grant number DE-FG02-93ER-40771, the Israeli Academy of Science, and the Australian Research Council.

## REFERENCES

- [1] L.L. Frankfurt, G.A. Miller, and M. Strikman, Ann. Rev. of Nucl. and Particle Phys. **44** (1994) 501.
- [2] H. Abramowicz, L. Frankfurt, and M. Strikman, report DESY-95-047; Proc. 22nd SLAC Summer Institute on Particle Physics, p. 539 (1994). Also in Surveys High Energ. Phys. **11** (1997) 51.
- [3] L. Frankfurt, Talk at the Workshop on Color Coherence in QCD, Grenoble, 1997.
- [4] M. Strikman, Lectures at LAFEX Int. School on High Energy Physics, Brasil, 1998.
- [5] J.C. Collins, L. Frankfurt, and M. Strikman, Phys. Rev. **D 56** (1997) 2982.
- [6] A. Radyushkin, Phys. Lett. **B 380** (1996) 417.
- [7] L. Frankfurt, W. Koepf, and M. Strikman, Phys. Rev. **D 54** (1996) 3194.
- [8] V.N. Gribov, B.L. Ioffe, and I.Y. Pomeranchuk, Sov. J. Nucl. Phys. **2** (1966) 549 (Yad. Fiz. **2** (1965) 768).
- [9] B.L. Ioffe, Phys. Lett. **B 30** (1969) 123.
- [10] V.N. Gribov, Sov. Phys. JETP **30** (1969) 709.
- [11] V.N. Gribov, Proc. of ITEP School on Elem. Particles, vol. 1, p.53, 1973.
- [12] L. Frankfurt and M. Strikman, Prog. Part. Nucl. Phys. **27**, 135 (1991).
- [13] L.D. Landau and I.Ya. Pomeranchuk, Comptes Rendus (Doklady) of the Acad. Sci. of the USSR **92** (1953) 535, 735.
- [14] H. Abramowicz and A. Caldwell, Rev. Mod. Phys. **71** (1999) 1275.
- [15] NMC Collab., P. Amaudruz, *et al.*, Nucl. Phys. **B 441** (1995) 3; M. Arneodo, *et al.*, ibid. **B 441** (1995) 12.
- [16] NMC Collab., M. Arneodo, *et al.*, Nucl. Phys. **B 481** (1996) 3; M. Arneodo, *et al.*, ibid. **B 481** (1996) 23.
- [17] L. Frankfurt and M. Strikman, Phys. Rep. **160** (1988) 235.
- [18] A.H. Mueller, Proc. 17th Recontre de Moriond, Moriond, ed. J. Tran Thanh Van (Gif-sur-Yvette: Editions Frontieres), France, 1982, vol. 1, p. 13.
- [19] S. Brodsky, Proc. 13th Int. Symp. on Multiparticle Dynamics, ed. W. Kittel, W. Metzger, and A. Stergiou (World Scientific: Singapore) 1982, p. 963.
- [20] H. A. Bethe and L. S. Maximon, Phys.Rev. **93** (1954) 768.
- [21] S.J. Brodsky, L. Frankfurt, J.F. Gunion, A.H. Mueller, and M. Strikman, Phys. Rev. **D 50** (1994) 3134.
- [22] L. Frankfurt, G.A. Miller, and M. Strikman, Phys. Lett. **B 304** (1993) 1.
- [23] E.M. Aitala *et al.* (E791 Collaboration), "Observation of color-transparency in diffractive dissociation of pions", preprint hep-ex/0010044; "Direct measurement of the pion valence quark momentum distribution, the pion light-cone wave function squared," preprint hep-ex/0010043; D. Ashery, Invited talk at Workshop on Physics with Electron Polarized Ion Collider - EPIC '99, Bloomington, IN, 8-11 Apr 1999. Published in *Bloomington 1999, Physics with a high luminosity polarized electron ion collider*, Edited by L.C. Bland, J.T. Lonergan, A.P. Szczepaniak (World Scientific: Singapore) 2000, pp. 322-334, also preprint hep-ex/9910024.
- [24] J.C Collins, Phys. Rev. **D 57** (1998) 3051.
- [25] V.N. Gribov, B.L. Ioffe, and I.Ya. Pomeranchuk, Phys. Lett. B 24 (1967) 554; V.N. Gribov, Sov. J. Nucl. Phys. **9** (1969) 369; V.N. Gribov, Sov. Phys. JETP **29** (1969) 483.
- [26] V. Abramovskii, V.N. Gribov, and O.V. Kancheli, Sov. J. Nucl. Phys. **18** (1974) 308.

- [27] L. Frankfurt and M. Strikman, Eur. Phys. J. **A 5** (1999) 293.
- [28] L. Alvero, L.L. Frankfurt, and M.I. Strikman, Eur. Phys. J. **A 5** (1999) 97.
- [29] E. Levin and M. Strikman, Sov. J. Nucl. Phys. **23** (1976) 216.
- [30] A. Capella, A. Kaidalov, C. Merino, D. Pertermann, and J. Tran Thanh Van, Eur. Phys. J. **C 5** (1998) 111.
- [31] L. Alvero, J. Collins, J. Terron, and J. Whitmore, Phys. Rev. **D 59** (1999) 074022.
- [32] L. Frankfurt, W. Koepf, and M. Strikman, Phys. Lett. **B 405** (1997) 367.
- [33] ZEUS Collab., J. Breitweg, *et al.*, Eur. Phys. J. **C 6** (1999) 43.
- [34] G. Piller and W. Weise, Phys. Rep. **330** (2000) 1.
- [35] H. Abramowicz, Rapporteur talk at the 19th Int. Symp. on Lepton and Photon Interactions at High Energies, Stanford University, August 9-14, 1999. Published in *eConf C990809, 2000*, pp. 495-520 and also in *Stanford 1999, Lepton and photon interactions at high energies*, Ed. J. Jaros and M. Peskin (World Scientific: Singapore) 2000, pp. 495-520; also preprint hep-ph/0001054.
- [36] B. Blättel, G. Baym, L.L. Frankfurt, and M. Strikman, Phys. Rev. Lett. **70** (1993) 896.
- [37] L. Frankfurt, A. Radyushkin, and M. Strikman, Phys. Rev. **D 55** (1997) 98.
- [38] M. McDermott, L. Frankfurt, V. Guzey, and M. Strikman, Eur. Phys. J. **C 16** (2000) 641.
- [39] F.E. Low, Phys. Rev. **D 12** (1975) 163; S. Nussinov, Phys. Rev. Lett. **34** (1975) 1286; J. Gunion and D. Soper, Phys. Rev. **D 15** (1977) 2617.
- [40] J.D. Bjorken, Proc. of the International Symposium on Electron and Photon Interactions at High Energies, p. 281–297, Cornell 1971; J.D. Bjorken and J.B. Kogut, Phys. Rev. **D 8** (1973) 1341.
- [41] Yu.L. Dokshitzer, V.A. Khoze, A.H. Mueller, and S.I. Troian, *Basics of perturbative QCD* (Gif-sur-Yvette: Editions Frontieres) 1991.
- [42] I.I. Balitsky and V.M. Braun, Nucl. Phys. **B 311** (1989) 541; A. Radyushkin, Phys. Lett. **B 385** (1996) 333; X.-D. Ji, Phys. Rev. **D 55** (1997) 7114.
- [43] L. Frankfurt, A. Freund, V. Guzey, and M. Strikman, Phys. Lett. **B 418** (1998) 345; Erratum-*ibid.* **B 429** (1998) 414.
- [44] A.V. Belitsky and D. Müller, Phys. Lett. **B 417** (1998) 129; A.V. Belitsky and D. Müller, Nucl. Phys. **B 527** (1998) 207; A.V. Belitsky and D. Müller, Nucl. Phys. **B 537** (1999) 397.
- [45] A.V. Belitsky, A. Freund, and D. Müller, Nucl. Phys. **B 574** (2000) 347.
- [46] A. Radyushkin, Phys. Lett. **B 449** (1999) 81.
- [47] A. Freund and V. Guzey, Phys. Lett. **B 462** (1999) 178.
- [48] G. Bertsch, S.J. Brodsky, A.S. Goldhaber, and J. Gunion, Phys. Rev. Lett. **B 47** (1981) 297.
- [49] E665 Collab., M.R. Adams *et al.*, Phys. Rev. Lett. **75** (1995) 1525.
- [50] M. Sokoloff *et al.*, Phys. Rev. Lett. **57** (1986) 3003.
- [51] L.L. Frankfurt and M. Strikman, Nucl. Phys. **B 250** (1985) 143.
- [52] L. Gerland, L. Frankfurt, M. Strikman, H. Stocker, and W. Greiner, Phys. Rev. Lett. **81** (1998) 762.
- [53] E791 Collab., E.M. Aitala *et al.*, Phys. Rev. Lett. **76** (1996) 364; E.M. Aitala *et al.*, Eur. Phys. J. **C 4** (1999) 1.
- [54] A.V. Efremov and A.V. Radyushkin, Theor. Math. Phys. **42** (1980) 97.

[55] S.J. Brodsky and G.P. Lepage, Phys. Rev. **D 22** (1980) 2157.

[56] L.L. Frankfurt and M. Strikman, Phys. Rev. Lett. **64** (1989) 1914; A.H. Mueller and W.K. Tang, Phys. Lett. **B 284** (1992) 123; L. Frankfurt, Materials of FAD meetings, 1992; M.G. Ryskin, Z. Phys. **C 37** (1993) 89; J. Bartels, H. Lotter, and M. Wusthoff, Phys. Lett. **B 378** (1996) 239.

[57] D. Schildknecht, Talk at 8th Intern. Workshop on Deep Inelastic Scattering and QCD (DIS 2000), Liverpool, England, April 2000, preprint hep-ph/0006153.

[58] L. Frankfurt, V. Guzey, and M. Strikman, Phys. Rev. **D 58** (1998) 094039.

[59] L. Frankfurt, A. Freund, and M. Strikman, Phys. Rev. **D 58** (1998) 114001; Erratum-ibid. **D 59** (1999) 119901.

[60] P.R.B. Saull (ZEUS Collaboration), Talk at EPS99, *Prompt Photon Production and Deeply Virtual Compton Scattering*, Tampere, Finland (July 1999); ZEUS homepage <http://www.zeus.desy.de>

[61] G. Shaw, *Phys. Rev. D 47* (1993) R3676; G. Shaw, *Phys. Lett. B 228* (1989) 125; P. Ditt-sas and G. Shaw *Nucl. Phys. 113* (1976) 246; H. Fraas, B. Read, and D. Schildknecht, *Nucl. Phys. B 86* (1975) 346.

[62] H. Lai *et al.*, Phys. Rev. **D 55** (1997) 1280.

[63] A. Freund and V. Guzey, preprint hep-ph/9801388.

[64] FELIX LoI, CERN/LHCC 97-45.

[65] M. Arneodo, A. Bialas, M.W. Krasny, T. Sloan, and M. Strikman, “Hamburg 1995/96, Future physics at HERA”, pp. 887-926.

[66] E. Feinberg and Ya. Pomeranchuk, Suppl. Nuovo Cimento **111** (1956) 652.

[67] M. Good and W. Walker, Phys. Rev. **D 120** (1960) 1857.

[68] H. Miettinen and J. Pumplin, Phys. Rev. **D 18** (1978) 1696.

[69] B. Blattel, G. Baum, L. Frankfurt, H. Heiselberg, and M. Strikman, Phys. Rev. **D 47** (1993) 2761.

[70] P. Murphy *et al.*, Nucl. Phys. **B 92** (1975) 269.

[71] L. Dakhno, Sov. J. Nucl. Phys. **37** (1983) 590.

[72] A. Carroll *et al.*, Phys. Lett. **B 61** (1976) 303.

[73] Y. Akimov *et al.*, Phys. Rev. Lett. **39** (1977) 1432; ibid. **40** (1978) 1159(E).

[74] R.J. Glauber, Phys. Rev. **100** (1955) 242.

[75] B. Kopeliovich and L. Lapidus, JETP Lett. **28** (1978) 614.

[76] B. Blattel, G. Baum, L. Frankfurt, and M. Strikman, Phys. Rev. Lett. **70** (1993) 896.

[77] A. Bujak *et al.*, Phys. Rev. **D 23** (1981) 1911.

[78] V. Guzey and M. Strikman, Phys. Rev. **C 52** (1995) 1189.

[79] V. Guzey, Ph.D. thesis, unpublished.

[80] L. Frankfurt, G. Miller, and M. Strikman, Phys. Rev. Lett. **71** (1993) 2859.

[81] M. Zielinski *et al.*, Z. Phys. **C 16** (1983) 197.

[82] E.G. Boos *et al.*, Nucl. Phys. **B 137** (1978) 37.

[83] H. Heiselberg, G. Baym, B. Blattel, L. Frankfurt, and M. Strikman, Phys. Rev. Lett. **67** (1991) 2946.

[84] F. Hautmann, Z. Kunszt, and D. E. Soper, Nucl. Phys. **B 563** (1999) 153, preprint hep-ph/9906284.

FIGURES

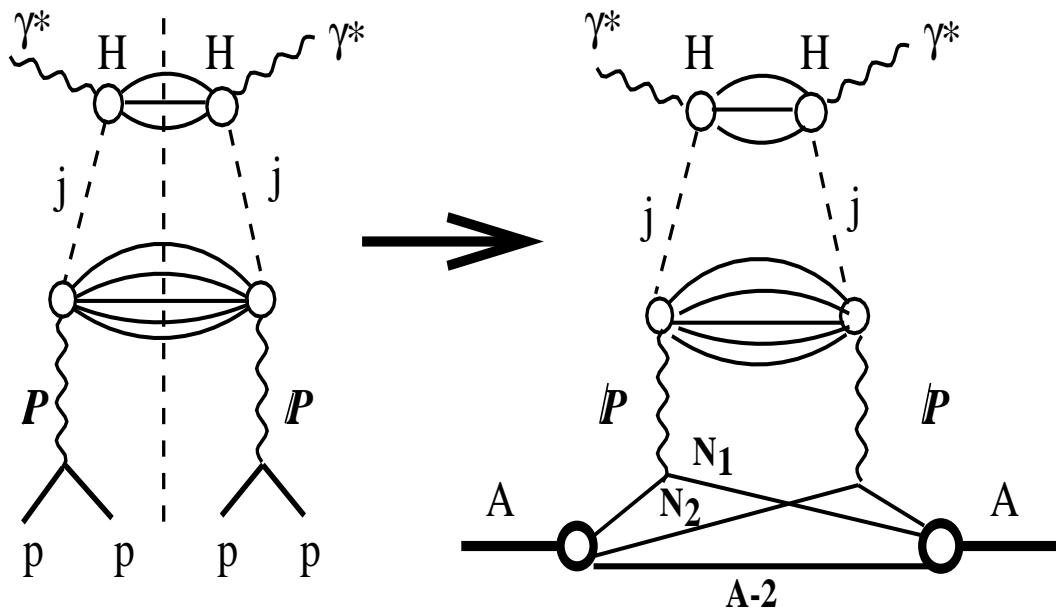


FIG. 1. Diagrams demonstrating the relationship between DIS diffraction on protons in the reaction  $\gamma^* + p \rightarrow X + p'$  and the leading contribution to nuclear shadowing in inclusive DIS on nuclei.

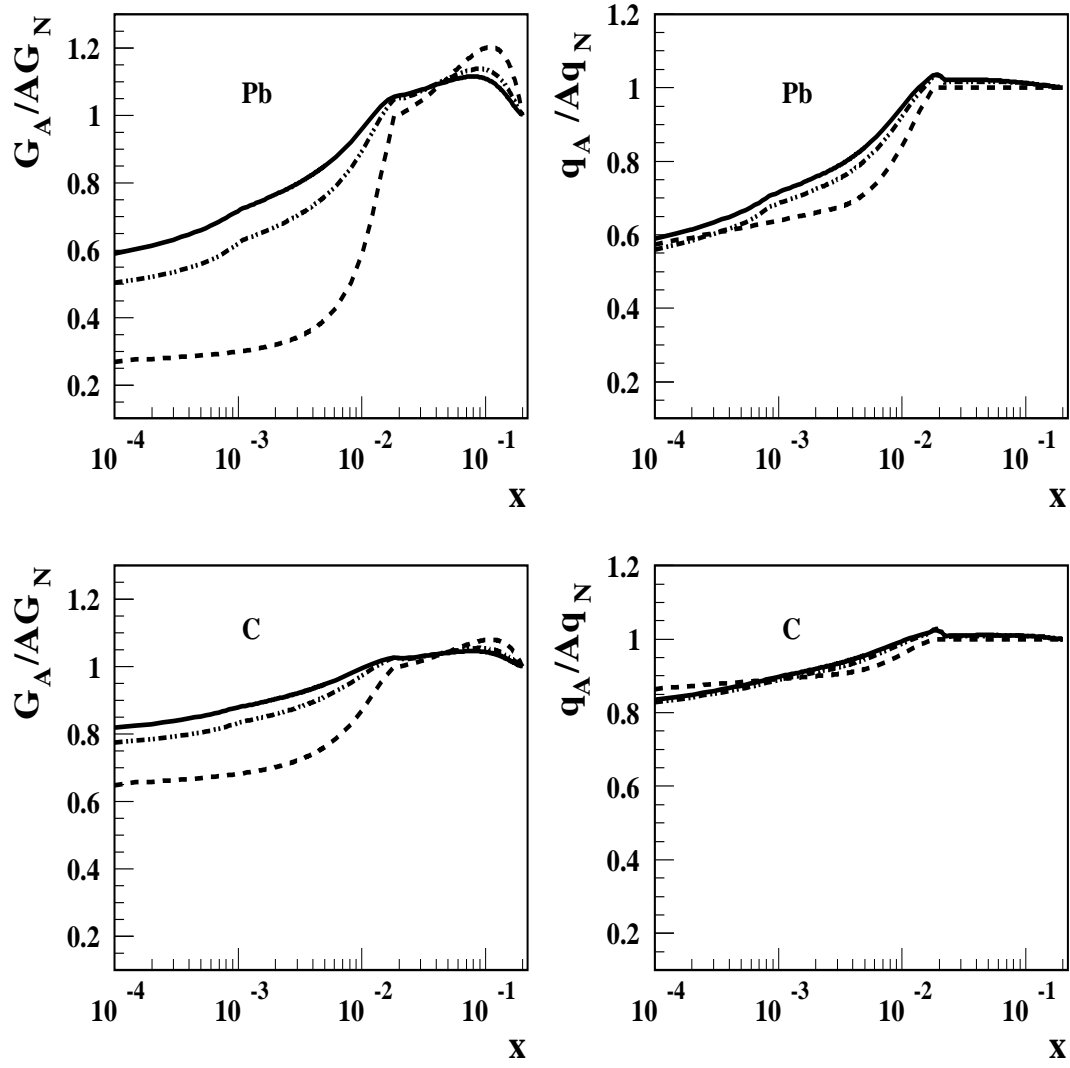


FIG. 2. The ratios of the nuclear and nucleon gluon parton densities  $G_A/\Delta G_N$  and the quark parton densities  $q_A/\Delta q_N$  for lead (Pb) and carbon (C) as a function of  $x$ . The dotted, dashed and solid curves correspond to  $Q=2, 5$  and  $10$  GeV, respectively.

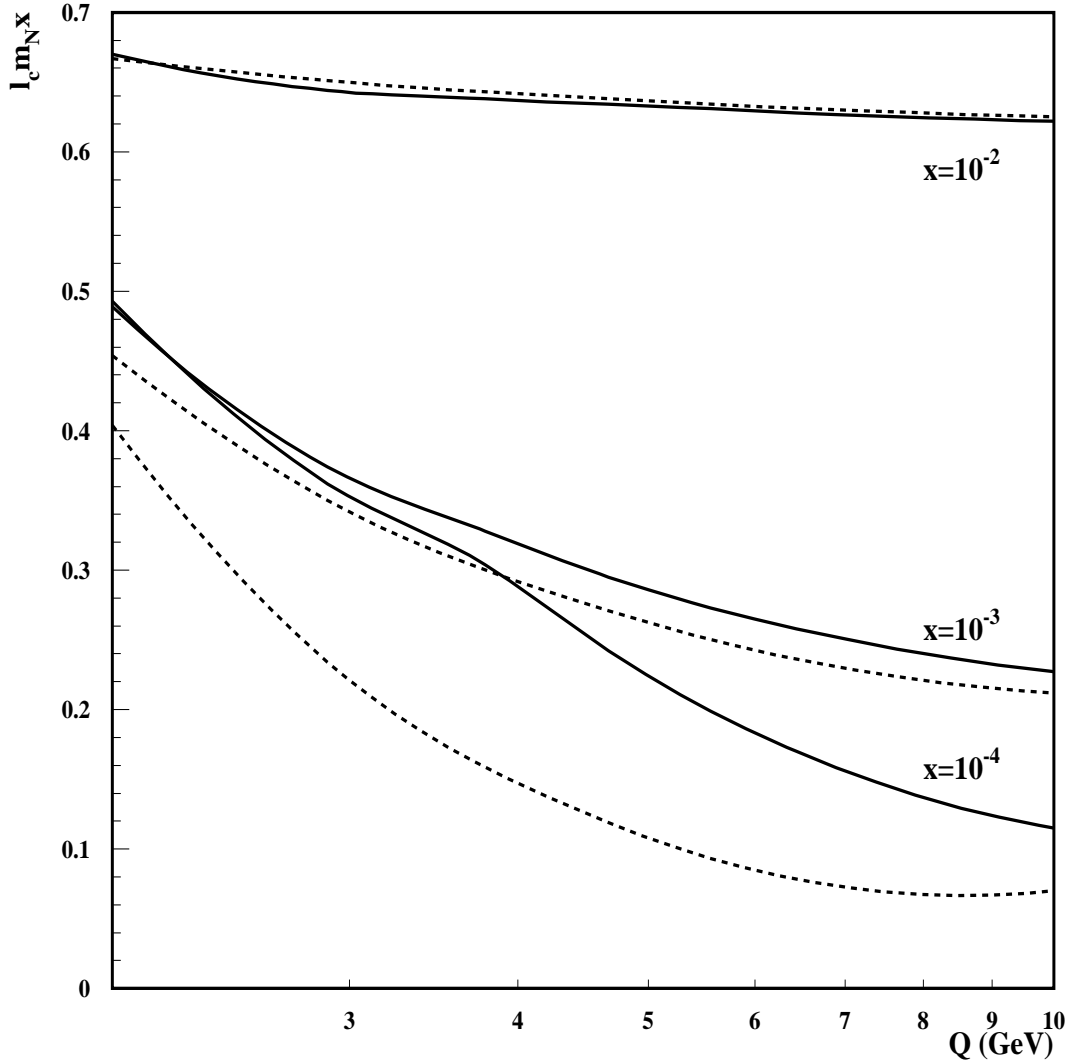


FIG. 3.  $l_c m_N x$  as a function of  $Q$  at  $x=10^{-4}$ ,  $10^{-3}$ , and  $10^{-2}$  as given by Eqs. (10) and (11). The solid curves correspond to the parameterization of the diffractive parton densities of [31]. The results, obtained with the parameterization, which also includes the low- $\beta$  tail (see explanation in the text), are given by the dashed curves.

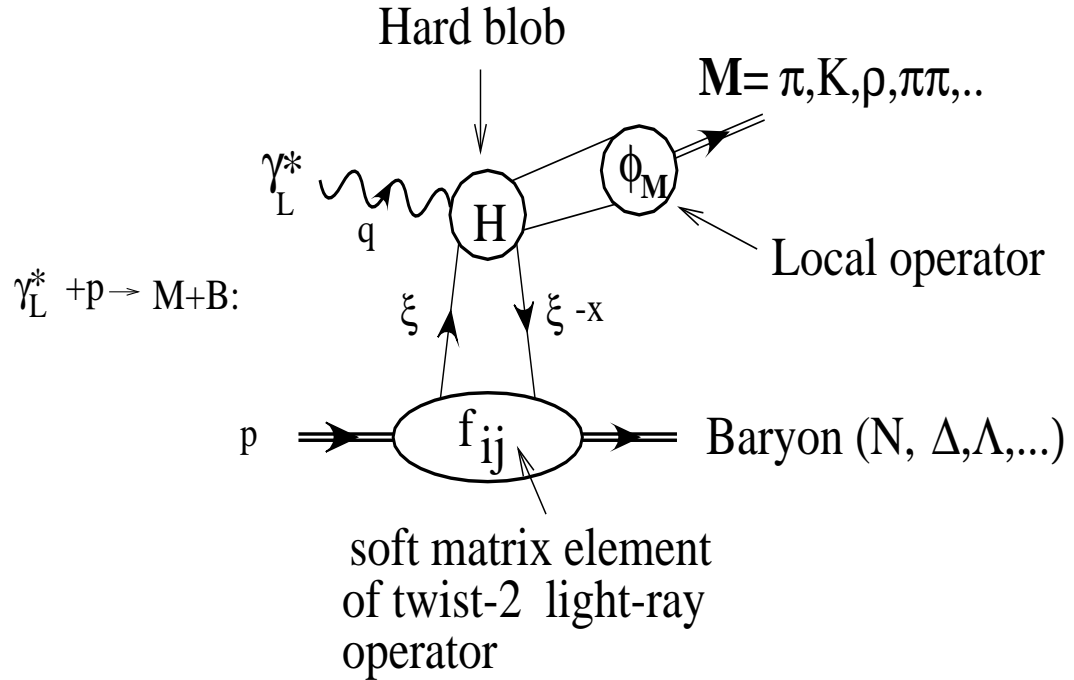


FIG. 4. The block structure of the amplitude for hard exclusive production of mesons  $M$  by longitudinally polarized photons  $\gamma_L^*$  in the reaction  $\gamma_L^* + p \rightarrow M + B$ , where  $p$  is proton and  $B$  is a baryon.

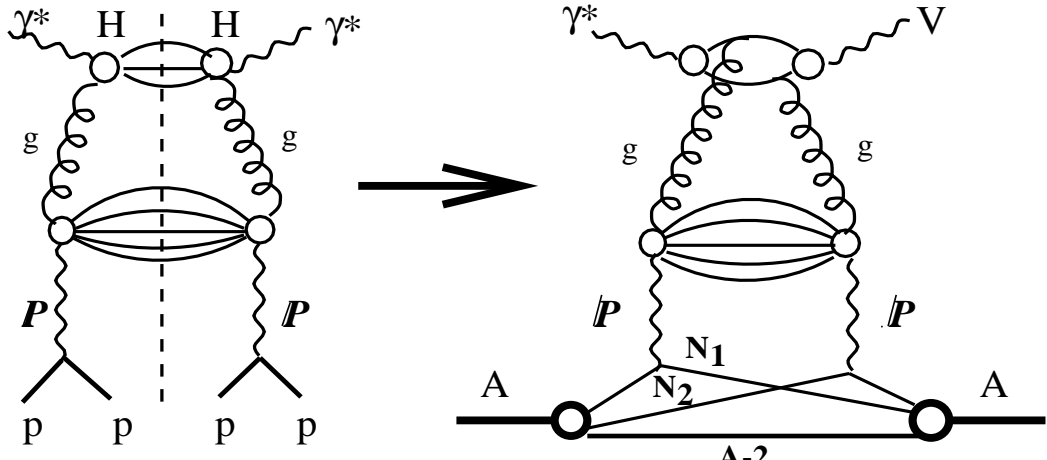


FIG. 5. Diagrams demonstrating the relationship between the gluon induced hard diffraction on protons and the leading twist contribution to nuclear shadowing in exclusive hard vector meson production in DIS on nuclei.

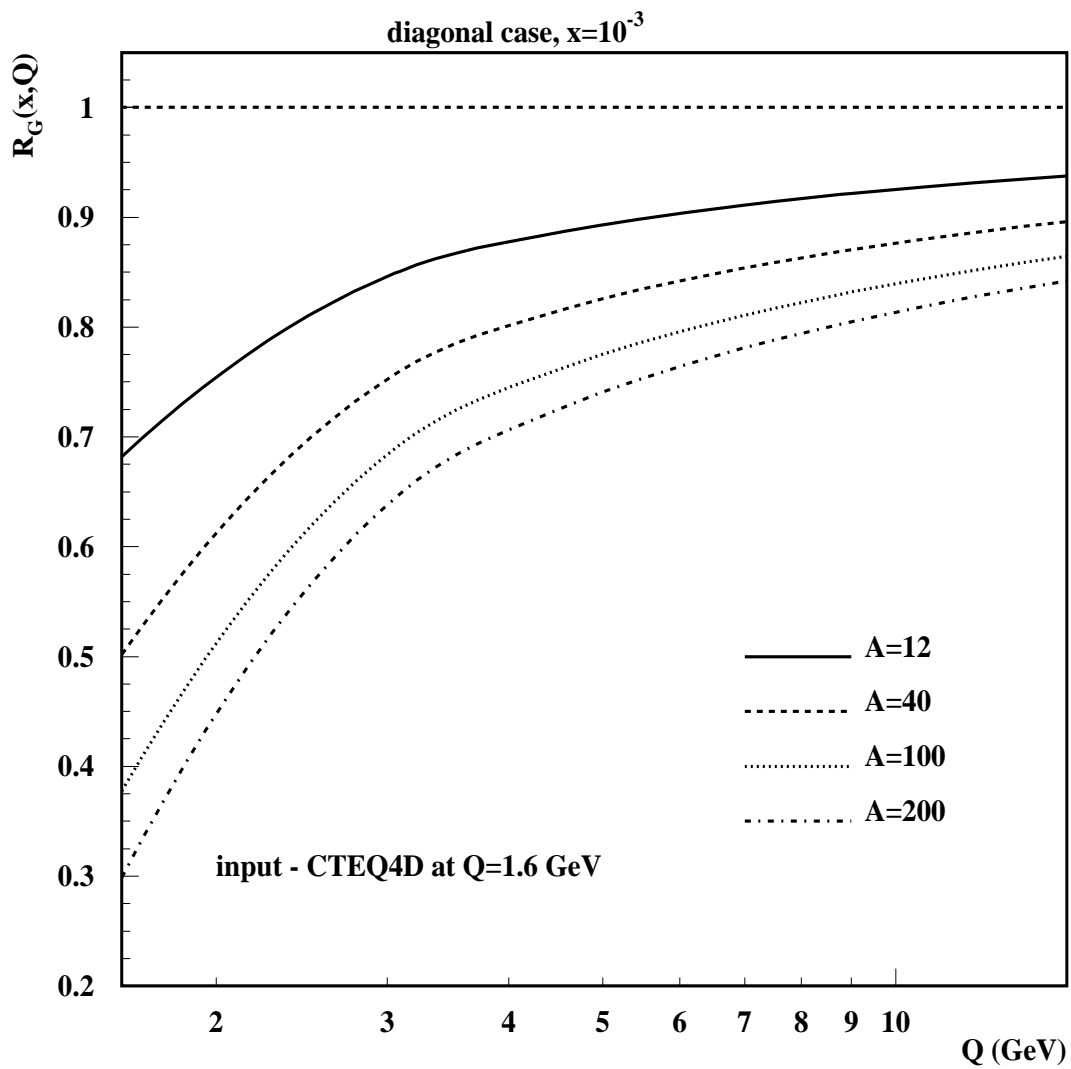


FIG. 6. The ratio of the conventional nuclear to nucleon gluon parton densities  $R_G(x, Q)$  as a function of  $Q$  at  $x=10^{-3}$ . The input distribution for the QCD evolution is CTEQ4D.

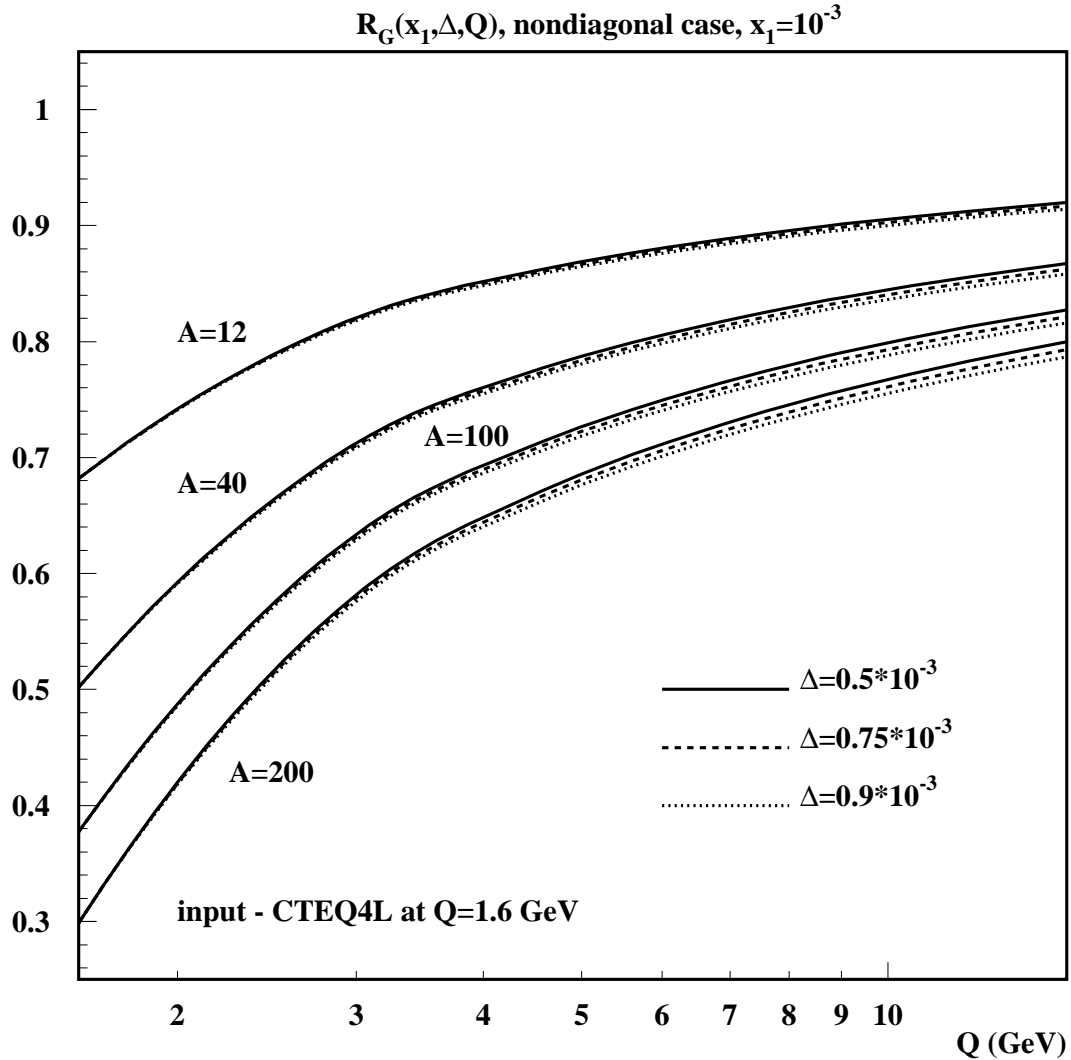


FIG. 7. The ratio of the skewed nuclear to nucleon gluon densities  $R_G(x_1, x_2, Q)$  as a function of  $Q$  at  $x_1=10^{-3}$  and at  $\Delta = 0.5 \times 10^{-3}$ ,  $\Delta = 0.75 \times 10^{-3}$  and  $\Delta = 0.9 \times 10^{-3}$ . The three curves for each  $\Delta$  are barely distinguishable. The input distribution for the QCD evolution is CTEQ4L.

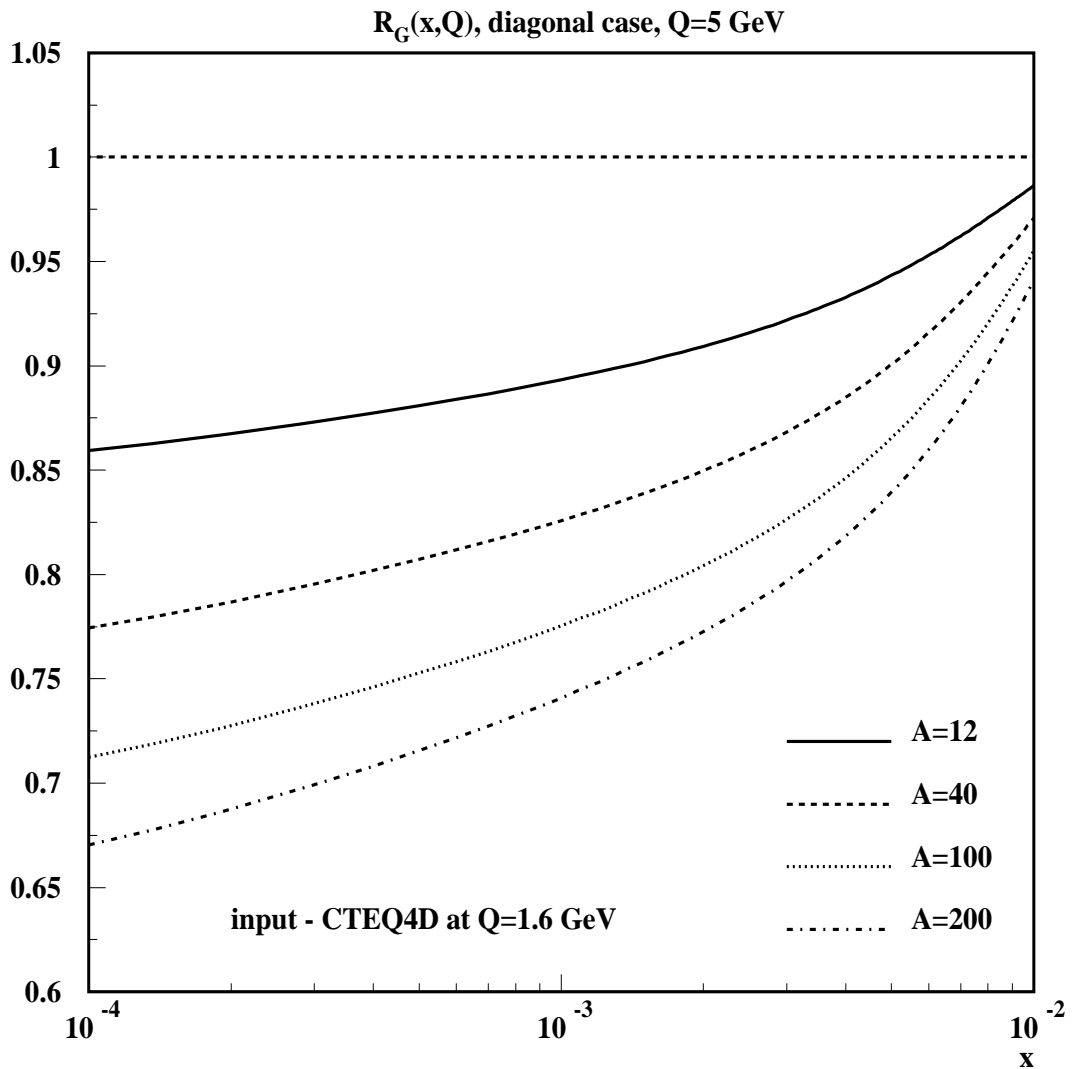


FIG. 8. The ratio of the conventional nuclear to nucleon gluon parton densities  $R_G(x, Q)$  as a function of  $x$  at  $Q=5$  GeV. The input distribution for the QCD evolution is CTEQ4D.

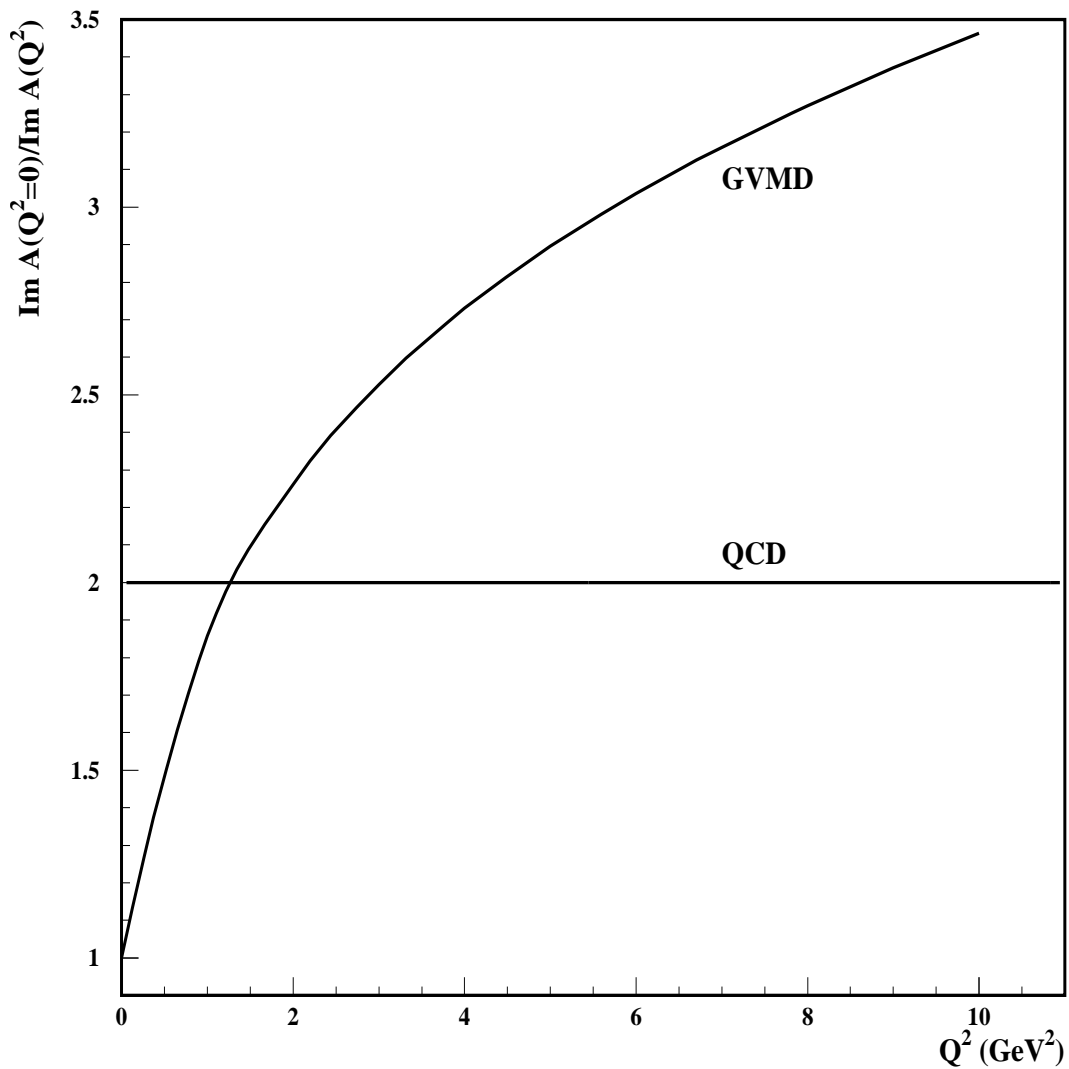


FIG. 9. The ratio of the imaginary parts of the amplitudes for real and virtual photon production by virtual photons as a function of  $Q^2$ . The straight line is the pQCD prediction [59]. The result of the calculation using the generalized vector meson dominance model (see Eq. (23) is given by curve.

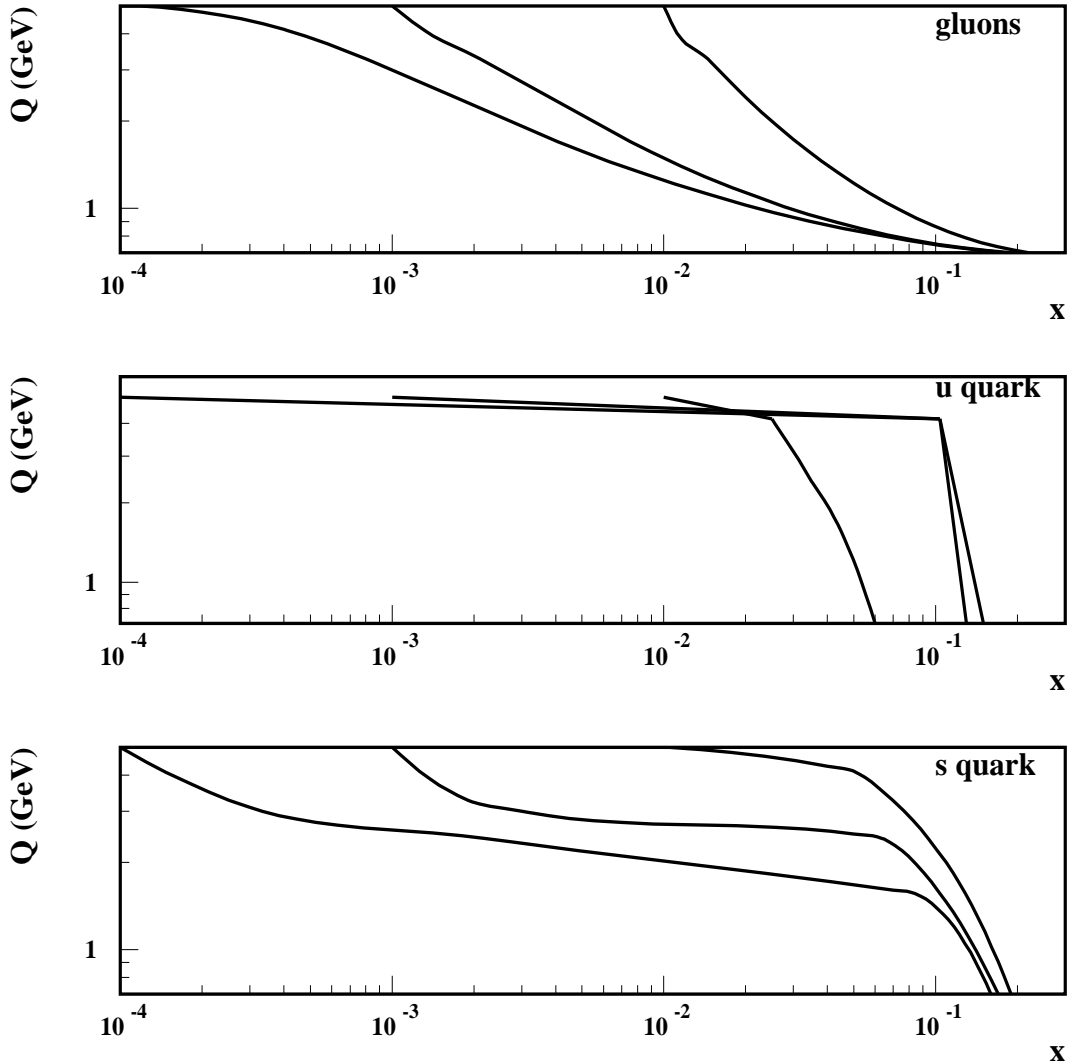


FIG. 10. The QCD evolution path in the  $x - Q$ -plane for the gluon,  $u$  quark, and  $s$  quark parton densities for the three final points,  $x = 10^{-4}, 10^{-3},$  and  $10^{-2}$ . CTEQ4LQ with  $Q_0=0.7$  GeV is used as an input for the QCD evolution.

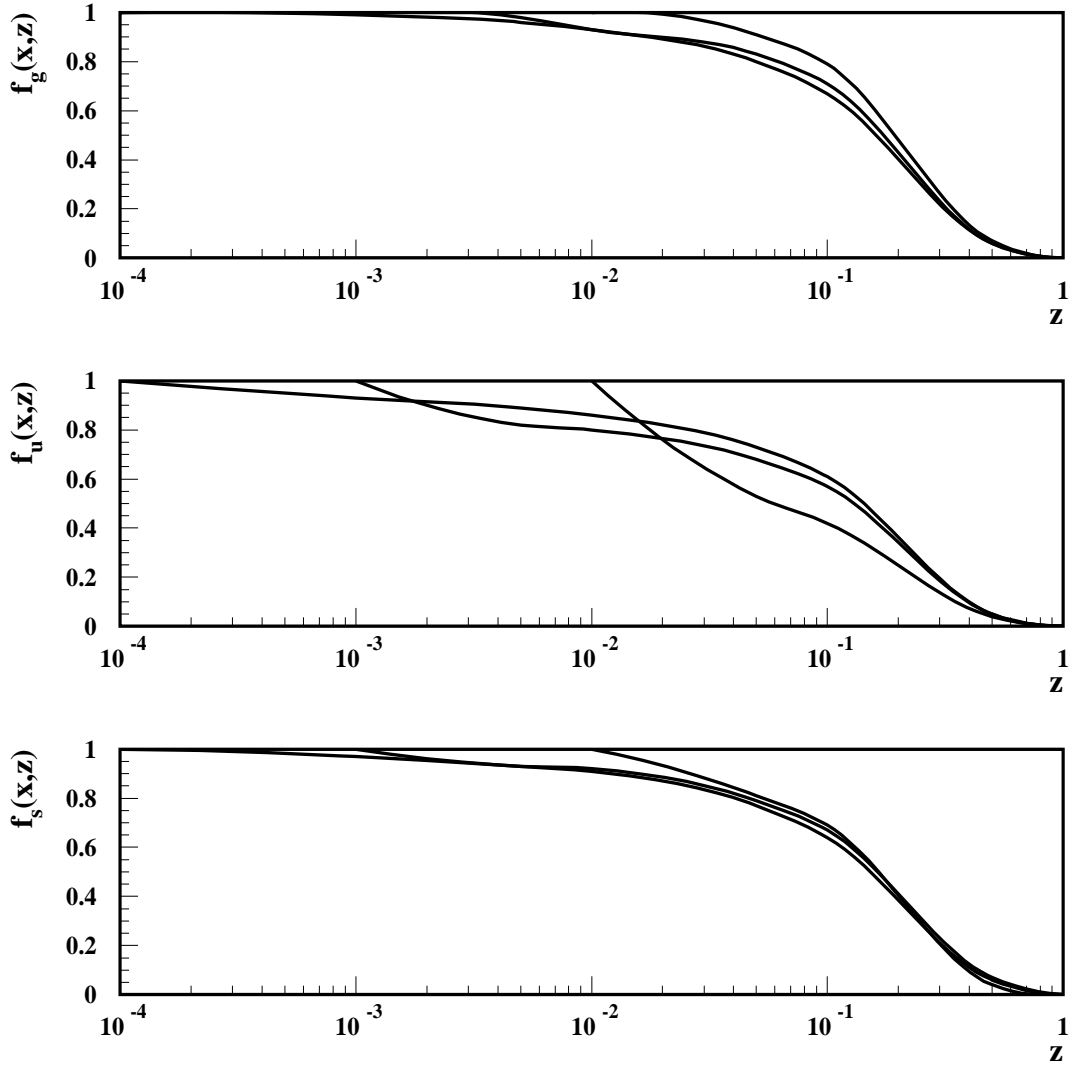


FIG. 11. Functions  $f(x, z)$  as a function of  $z$  and at  $x = 10^{-4}, 10^{-3}$ , and  $10^{-2}$  for the gluon,  $u$  quark, and  $s$  quark parton densities. CTEQ4LQ with  $Q_0=0.7$  GeV is used as an input for the QCD evolution.

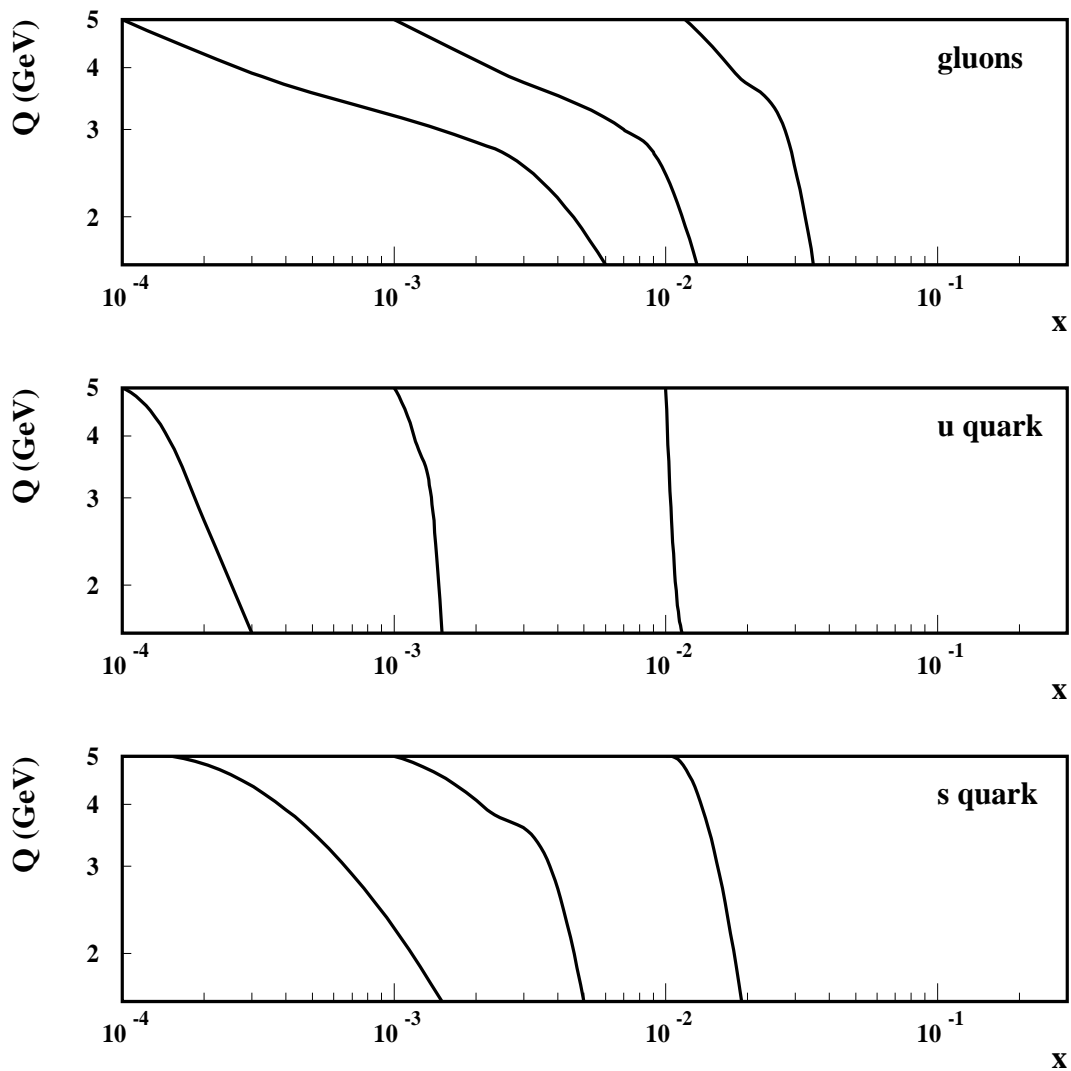


FIG. 12. The QCD evolution path in the  $x - Q$ -plane for the gluon,  $u$  quark, and  $s$  quark parton densities for the three final points,  $x = 10^{-4}$ ,  $10^{-3}$ , and  $10^{-2}$ . CTEQ4D with  $Q_0=1.6$  GeV is used as an input for the QCD evolution.

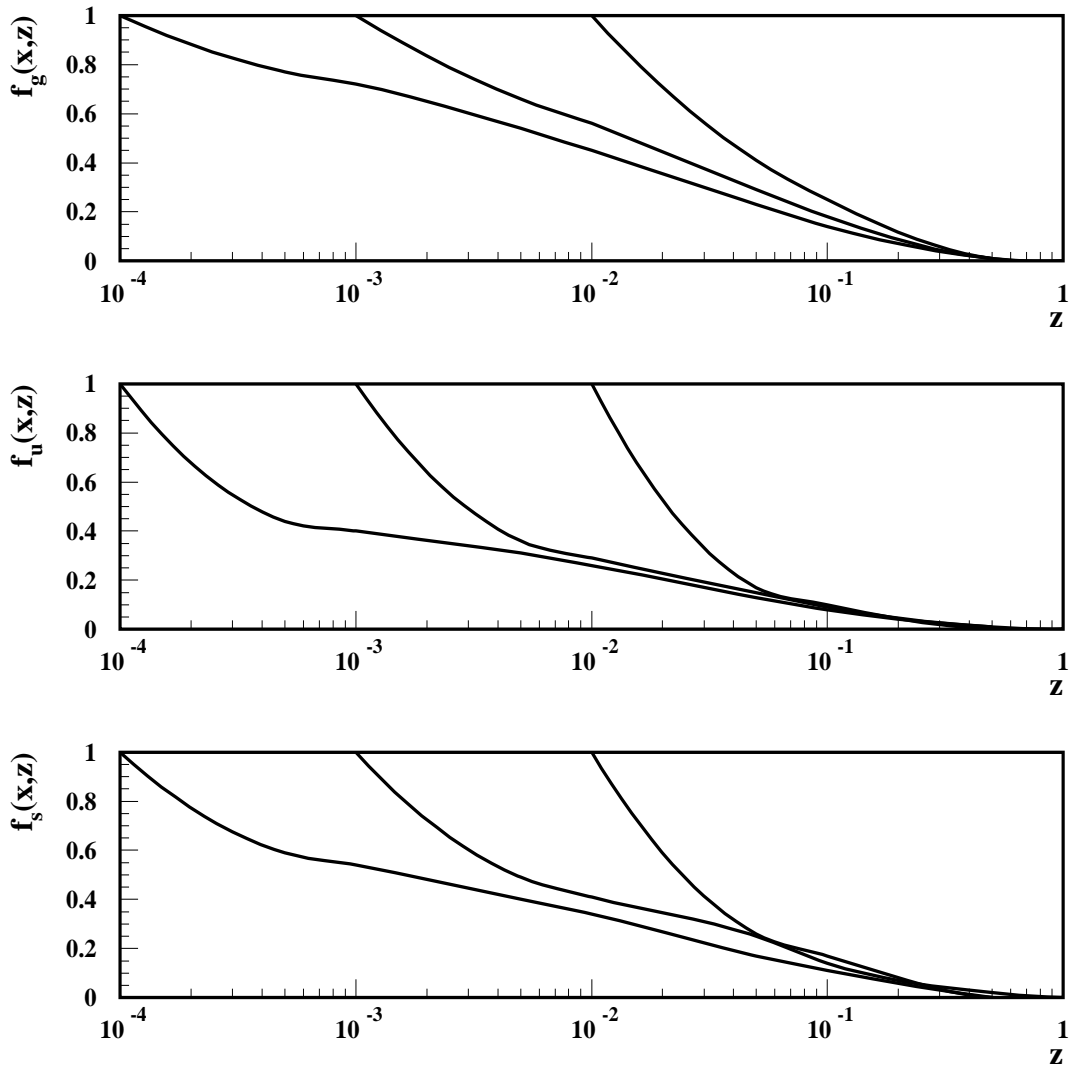


FIG. 13. Functions  $f(x,z)$  as a function of  $z$  and at  $x = 10^{-4}, 10^{-3}$ , and  $10^{-2}$  for the gluon,  $u$  quark, and  $s$  quark parton densities. CTEQ4D with  $Q_0=1.6$  GeV is used as an input for the QCD evolution.

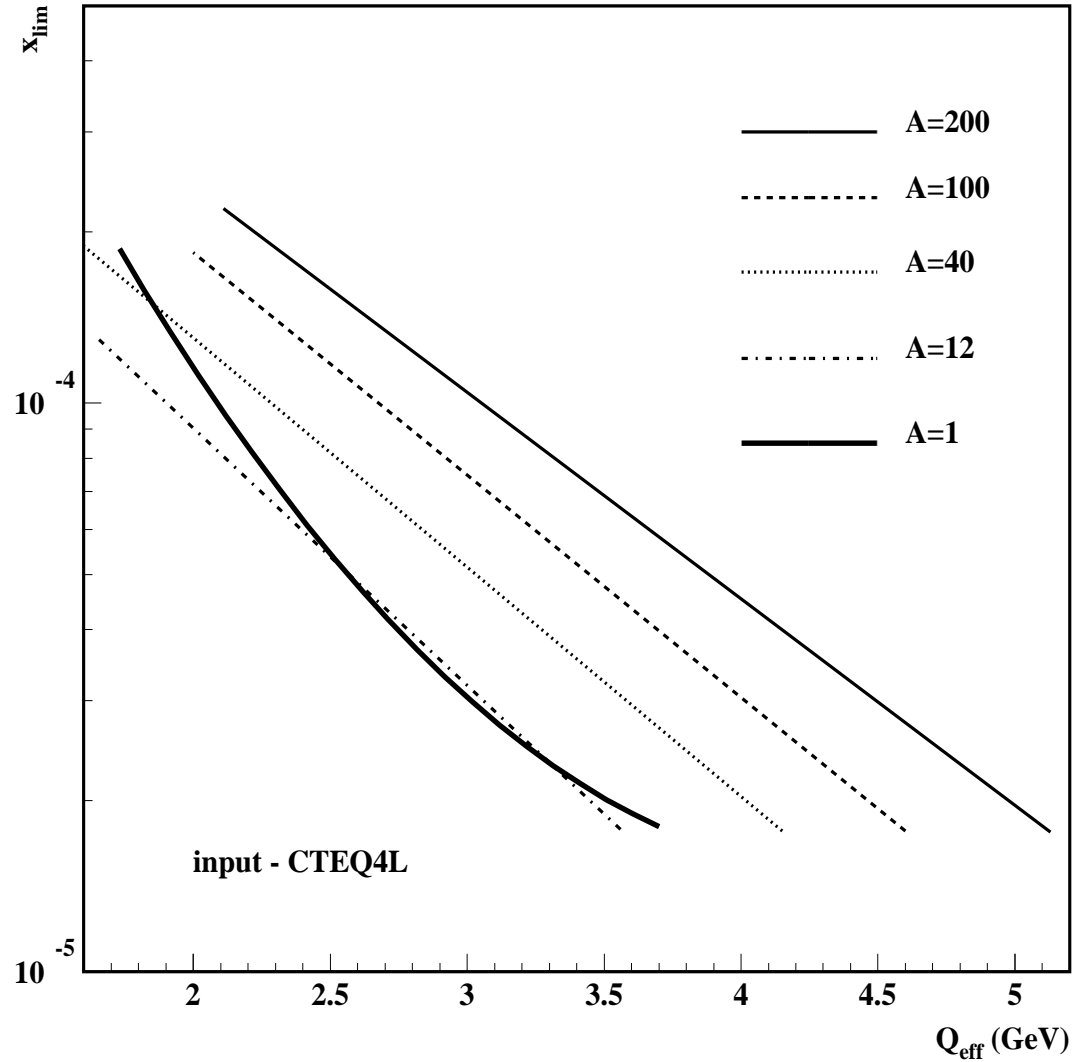


FIG. 14. The unitarity boundary for the inelastic  $q\bar{q}$ -nucleus cross sections for nuclei with  $A=12$ , 40, 100, and 200. The unitarity boundary for the inelastic  $q\bar{q}$ -nucleon cross section is presented as a thick solid curve.

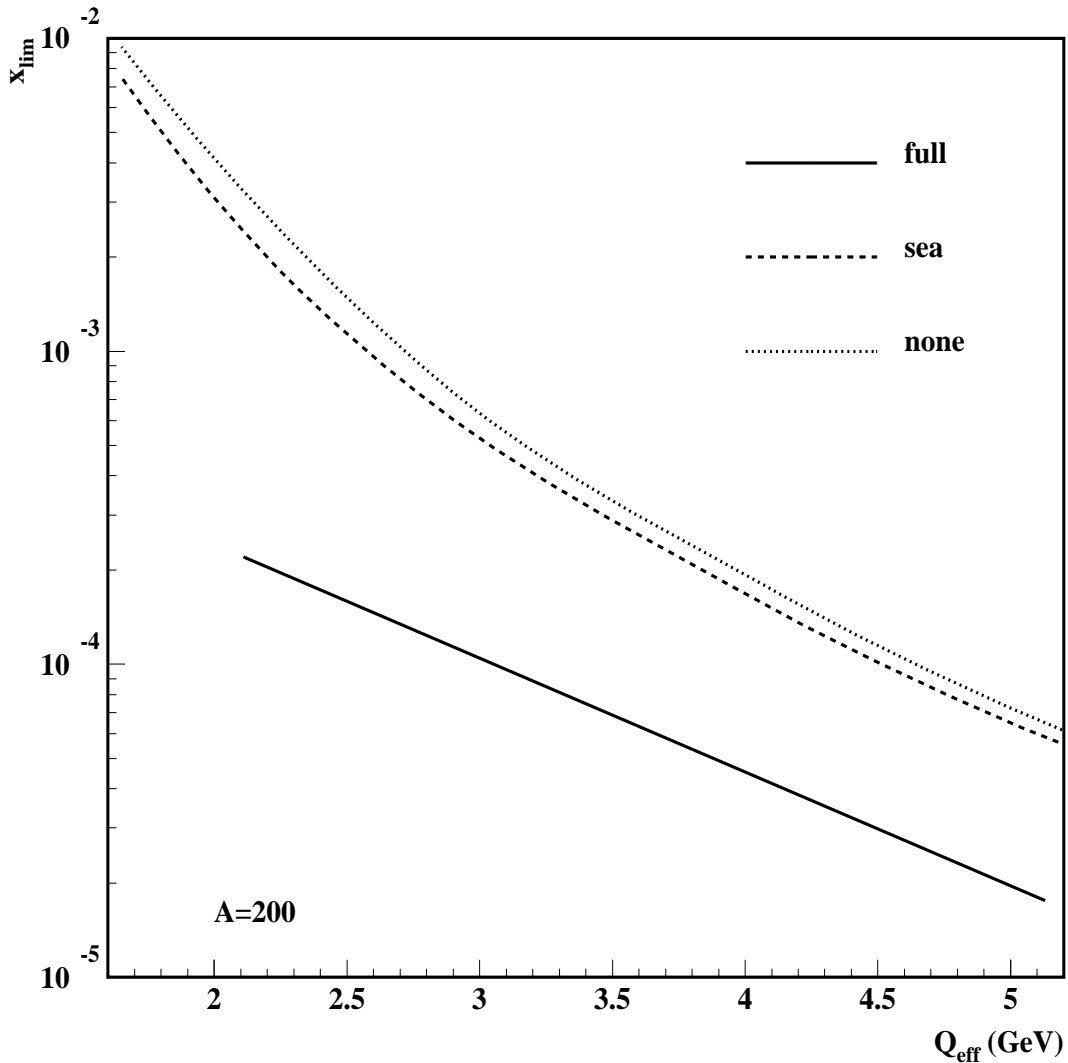


FIG. 15. The unitarity boundary for the inelastic  $q\bar{q}$ -nucleus cross sections for nuclei with  $A=200$ . The amount of nuclear shadowing for gluons is varied: the solid curve corresponds to the full amount of shadowing, the dashed curve corresponds to the gluons shadowed as the sea quarks, and the dotted curve is for gluons without shadowing.

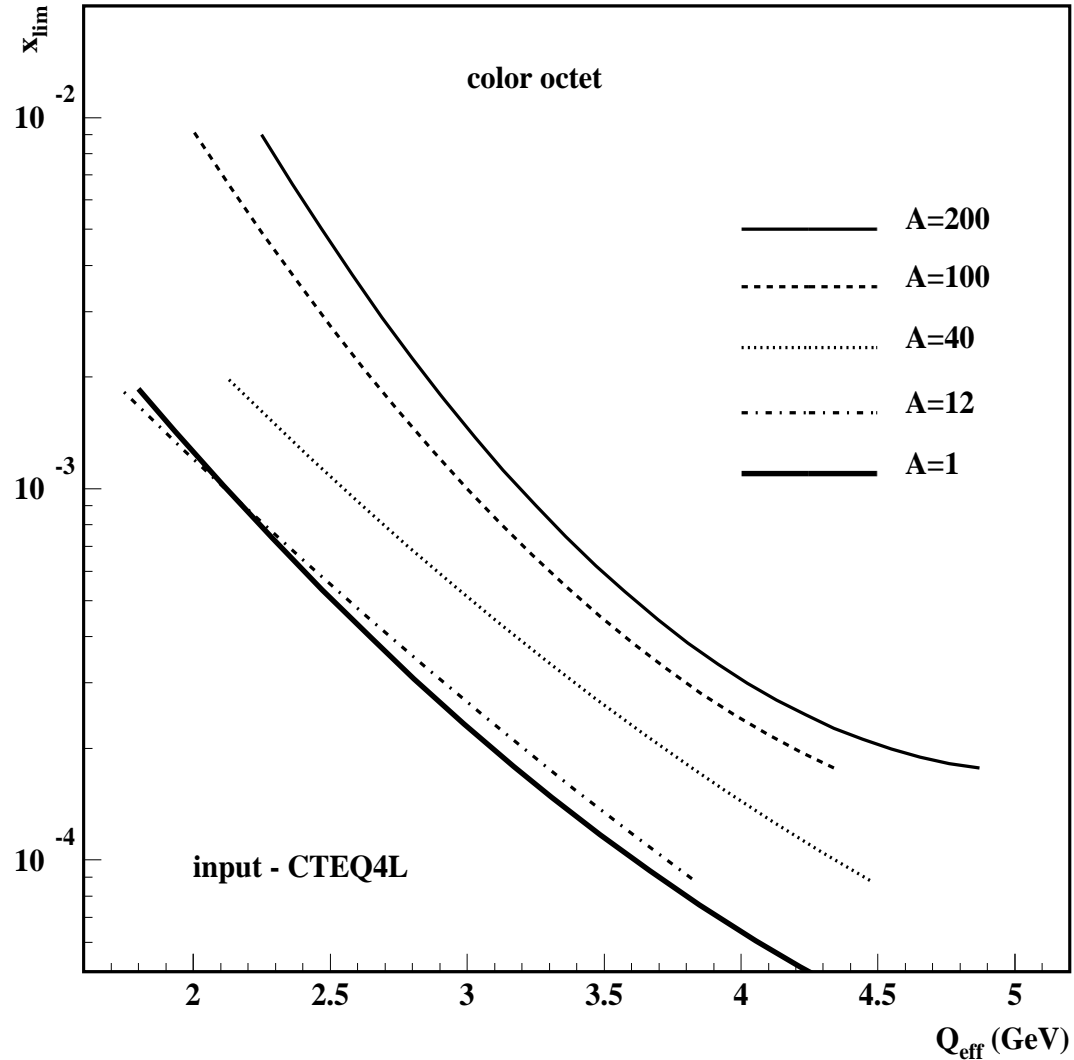


FIG. 16. The unitarity boundary for the inelastic  $q\bar{q}g$  (color octet)-nucleus cross sections for nuclei with  $A=12, 40, 100$ , and  $200$ . The unitarity boundary for the inelastic  $q\bar{q}g$ -nucleon cross section is presented as a thick solid curve.

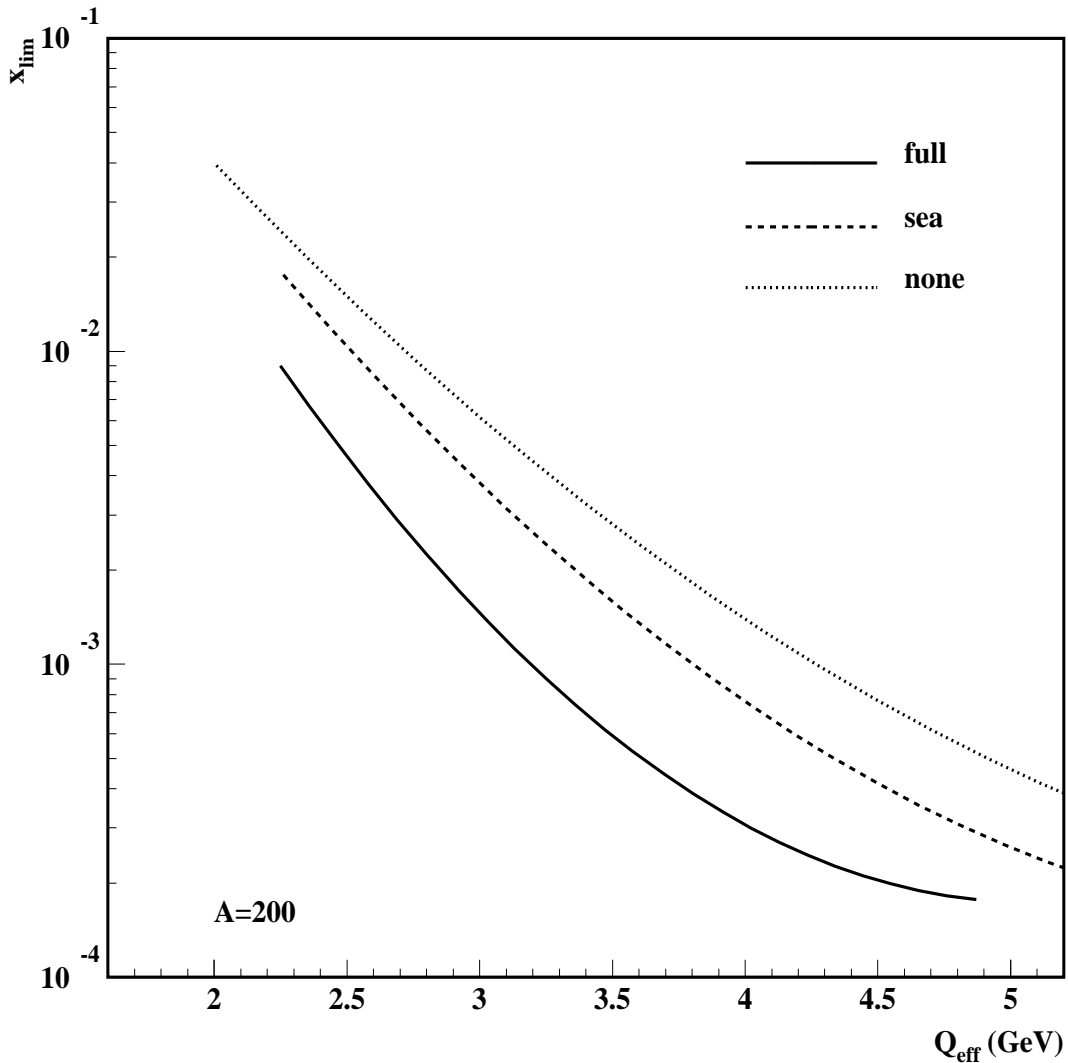


FIG. 17. The unitarity boundary for the inelastic  $q\bar{q}g$  (color octet)-nucleus cross sections for nuclei with  $A=200$ . The amount of nuclear shadowing for gluons is varied: the solid curve corresponds to the full amount of shadowing, the dashed curve corresponds to the gluons shadowed as the sea quarks, and the dotted curve is for gluons without shadowing.

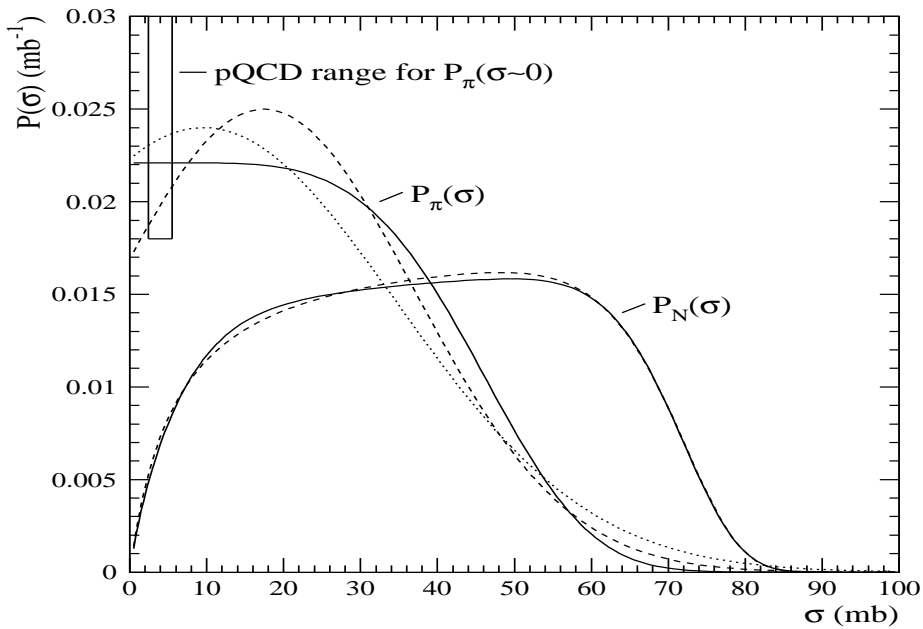


FIG. 18. The distribution over cross sections  $P(\sigma)$  for protons and pions, presented in Eq. (47).

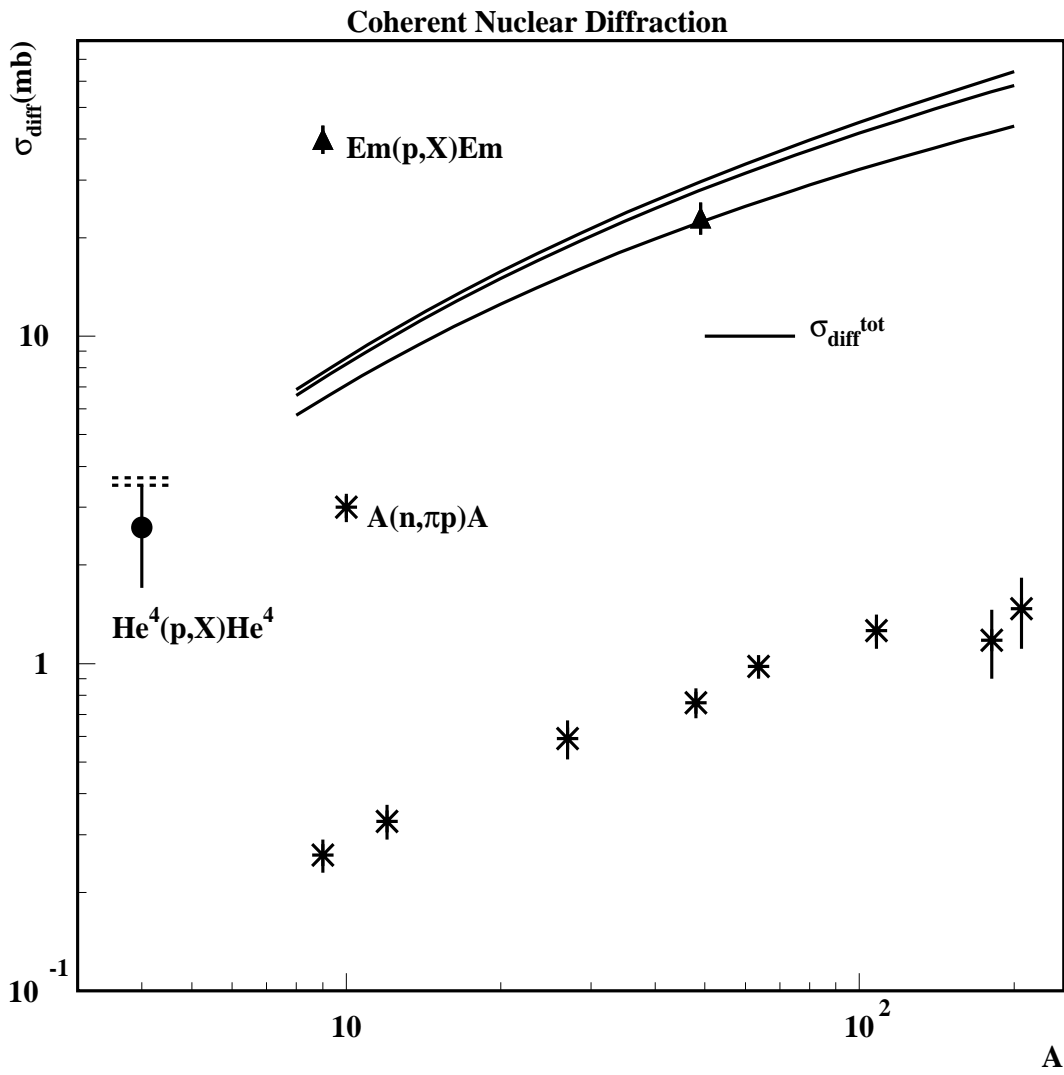


FIG. 19. The cross section of coherent diffraction dissociation of protons and neutrons on nuclei as a function of the atomic number  $A$ . The solid curves are the theoretical prediction of Eq. (59). The data on the reaction  $n + A \rightarrow p\pi^- + A$  [81] is presented as stars and the data for the emulsion targets [82] is presented as triangles. The data point, presented by the full circle, corresponds to  $A = 4$  ( ${}^4\text{He}$ ) and is extracted from [77] (see Eq. (58)). The theoretical prediction for coherent diffraction on  ${}^4\text{He}$  is given by the dashed curves (see Eq. (57)).